J. Fluid Mech. (2023), *vol*. 976, A6, doi:10.1017/jfm.2023.890

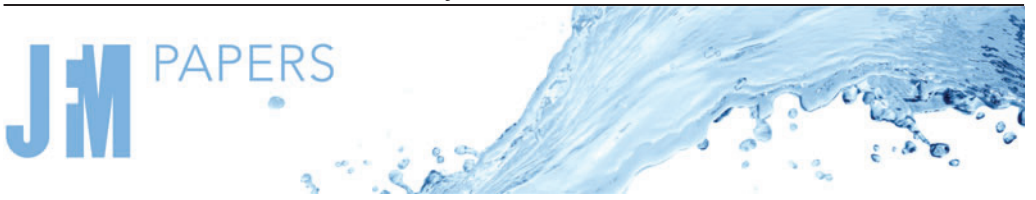

Laminar post-stall wakes of tapered swept wings

Jean Hélder Marques Ribeiro[1],†, **Jacob Neal**[2],‡, **Anton Burtsev**[3],‡, **Michael Amitay**[2], **Vassilios Theofilis**[3],§ **and Kunihiko Taira**[1]

[1]Department of Mechanical and Aerospace Engineering, University of California, Los Angeles, CA 90095, USA

[2]Department of Mechanical, Aeronautical, and Nuclear Engineering, Rensselaer Polytechnic Institute, Troy, NY 12180, USA

[3]Department of Mechanical and Aerospace Engineering, University of Liverpool, Brownlow Hill, Liverpool L69 3GH, UK

(Received 12 April 2023; revised 4 October 2023; accepted 19 October 2023)

While tapered swept wings are widely used, the influence of taper on their post-stall wake characteristics remains largely unexplored. To address this issue, we conduct an extensive study using direct numerical simulations to characterize the wing taper and sweep effects on laminar separated wakes. We analyse flows behind NACA 0015 cross-sectional profile wings at post-stall angles of attack $\alpha = 14^\circ$–22° with taper ratios $\lambda = 0.27$–1, leading-edge sweep angles 0°–50° and semi aspect ratios $sAR = 1$ and 2 at a mean-chord-based Reynolds number of 600. Tapered wings have smaller tip chord length, which generates a weaker tip vortex, and attenuates inboard downwash. This results in the development of unsteadiness over a large portion of the wingspan at high angles of attack. For tapered wings with backward-swept leading edges, unsteadiness emerges near the wing tip. On the other hand, wings with forward-swept trailing edges are shown to concentrate wake-shedding structures near the wing root. For highly swept untapered wings, the wake is steady, while unsteady shedding vortices appear near the tip for tapered wings with high leading-edge sweep angles. For such wings, larger wake oscillations emerge near the root as the taper ratio decreases. While the combination of taper and sweep increases flow unsteadiness, we find that tapered swept wings have more enhanced aerodynamic performance than untapered and unswept wings, exhibiting higher time-averaged lift and lift-to-drag ratio. The current findings shed light on the fundamental aspects of flow separation over tapered wings in the absence of turbulent flow effects.

Key words: vortex dynamics, wakes, separated flows

† Present address: Faculdade de Engenharia Mecânica, Universidade Estadual de Campinas, Campinas, SP 13083-860, Brazil. Email address for correspondence: jeanmarques@g.ucla.edu
‡ Present address: Department of Aerospace Engineering and Engineering Mechanics, The University of Texas at Austin, Austin, TX 78712, USA.
§ Present address: Faculty of Aerospace Engineering, Technion - Israel Institute of Technology, Haifa 32000, Israel.

1. Introduction

Flow separation over aerodynamic lifting bodies has been a subject of research interest for decades, especially for small-scale air vehicles (Mueller 2001; Anderson 2010). To further understand the post-stall wake dynamics, it is important to analyse the influence of wing planform geometry. This characterization is challenging for high-Reynolds-number flows, due to the multiscale nature of the wakes. Nevertheless, for massively separated flows, the large vortex structures observed in higher-Reynolds-number flows are topologically analogous to the core structures in low-Reynolds-number flows (Hunt *et al.* 1978; Dallmann 1988; Délery 2001). To examine the fundamental aspects of unsteady three-dimensional (3-D) flow separation, we study post-stall flows in the absence of turbulence (Taira & Colonius 2009; Zhang *et al.* 2020*a*,*b*). This characterization has been largely unexplored for low-Reynolds-number flows over tapered wings.

In aircraft design, tapered wings are used to approximate the elliptic aerodynamic loading over the wingspan. Tapered wings are more feasible to manufacture due to their less complex geometry compared with elliptic wings (Prandtl 1920; McCormick 1995). The usage of tapered wings in aeronautics led to initial studies that explored the wing taper effect, especially for high-Reynolds-number flows (Anderson 1936; Millikan 1936; Irving 1937; Soule & Anderson 1940; Falkner 1950). For the laminar flow regime, the effect of wing taper on the wake dynamics is critical as the local Reynolds number is drastically reduced near the tip. For flows over wings at a chord-based Reynolds number $Re_c = O(10^4)$, taper affects the aerodynamic loading with an increase in the pressure drag (Traub 2013; Traub *et al.* 2015). For $Re_c = O(10^3)$, the aerodynamic characteristics are affected significantly by the viscous effects and the influence of wing taper on the wakes remains elusive, especially for massively separated flows.

Post-stall wake dynamics has attracted the attention of aeronautical researchers for many decades. The early efforts to understand post-stall flows over wings were performed over two-dimensional (2-D) spanwise homogeneous wings (Abbott & Von Doenhoff 1959; Gaster 1967; Tobak & Peake 1982). Valuable insights were obtained from 2-D analysis characterizing the behaviour of the separated laminar boundary layer (Horton 1968) and describing the relation between vortex-shedding structures, adverse pressure gradient and shear-layer characteristics (Pauley, Moin & Reynolds 1990). Moreover, the emergence of wake patterns associated with 3-D separation bubbles, as predicted in topological studies (Hornung & Perry 1984; Perry & Hornung 1984), was shown by global linear stability analysis to arise from self-excitation of the laminar separation bubble (Theofilis, Hein & Dallmann 2000).

The analysis of 2-D flows around canonical wings continues providing fundamental insights into the effect of angle of attack and Reynolds number on the wake-shedding structures (Lin & Pauley 1996; Huang *et al.* 2001; Yarusevych, Sullivan & Kawall 2009; Rossi *et al.* 2018; Durante, Rossi & Colagrossi 2020). For separated flows, an increase in Reynolds number and the angle of attack yields a 3-D flow field even around infinite and spanwise homogeneous wings (Bippes & Turk 1980; Winkelman & Barlow 1980; Braza, Faghani & Persillon 2001; Schewe 2001; Hoarau *et al.* 2003; Pandi & Mittal 2019). In such cases, spanwise fluctuations emerge, producing 3-D vortices in the wake, as a result of the growth of 3-D structures associated with secondary linear instability (He *et al.* 2017*a*).

For finite wings, 3-D wakes result from tip effects, as a strong streamwise vortex is formed rolling up around the wing tip (Winkelman & Barlow 1980; Freymuth, Finaish & Bank 1987; Toppings & Yarusevych 2022). While turbulence has an important influence on the 3-D wake (Pandi & Mittal 2019), some of the core global flow structures remain coherent over a broad range of Reynolds numbers, including the quasi-spanwise midspan

shedding and the tip vortex (Neal & Amitay 2023; Pandi & Mittal 2023). Tip vortices induce downwash inboard over the wing, which reduces the effective angle of attack near the tip, even suppressing stall formation (Dong, Choi & Mao 2020; Toppings & Yarusevych 2021) and the wake shedding for low-aspect-ratio wings (Taira & Colonius 2009; Zhang *et al.* 2020*b*). The tip vortex has been extensively studied to reveal its influence on the wake dynamics, aerodynamic forces and pitch moments (Francis & Kennedy 1979; Green & Acosta 1991; Devenport *et al.* 1996; Pelletier & Mueller 2000; Birch *et al.* 2004; Torres & Mueller 2004; Buchholz & Smits 2006; Yilmaz & Rockwell 2012; Ananda, Sukumar & Selig 2015; He *et al.* 2017*b*). Beyond understanding the tip vortex formation and evolution, a characterization of its instabilities has enabled the development of control techniques that improve the aerodynamic performance around finite wings (Edstrand *et al.* 2018; Gursul & Wang 2018; Navrose, Brion & Jacquin 2019).

Wing sweep also has a strong influence on post-stall wake dynamics. For laminar flow regimes, a number of experimental and numerical efforts were made to examine the effects of backward and forward wing sweep (Yen & Hsu 2007; Yen & Huang 2009; Zhang *et al.* 2020*a*) and identify global modes (Burtsev *et al.* 2022; Ribeiro, Yeh & Taira 2023*b*) that give rise to fundamental global coherent structures of flow separation around swept wings. It is noteworthy that some of the wing-sweep effects on laminar post-stall flows are topologically analogous over a wide range of Reynolds numbers. For instance, for low-Reynolds-number flows over swept wings, some of the core coherent structures emerging in the near wake, such as the 'ram's horn' vortex and the canard leading-edge vortices, were also identified in experiments performed at higher Reynolds numbers (Black 1956; Breitsamter & Laschka 2001; Neal *et al.* 2023*a*). Moreover, the stabilizing effect of the sweep-induced spanwise flow on the wake structures, which significantly impacts stall characteristics, as observed at low-Reynolds-number flows (Zhang *et al.* 2020*a*; Ribeiro *et al.* 2022, 2023*b*), is further noticed in both experiments and high-fidelity large-eddy simulations performed at a higher-Reynolds-number regime (Harper & Maki 1964; Visbal & Garmann 2019).

The aforementioned studies highlight the importance of the low-Reynolds-number post-stall wake characterization for revealing fundamental aspects of the unsteady 3-D flow separation physics. In fact, the insights obtained from studies of post-stall laminar flows have been important for expanding our knowledge of the stalled flow physics over a wide range of Reynolds numbers. Thus far, however, most studies have not considered wing-taper effects on low-Reynolds-number flows at high angles of attack. Only recently, a combined experimental, numerical and theoretical effort has been initiated towards the understanding of the laminar flow over tapered wings in post-stall flow conditions (Burtsev *et al.* 2023; Neal *et al.* 2023*b*; Ribeiro *et al.* 2023*a*). Effects of taper have been analysed for planforms with tubercles to analyse swimming of whales (Wei, New & Cui 2018), for flows over tapered cylinders (Piccirillo & Van Atta 1993; Techet, Hover & Triantafyllou 1998; Valles, Andersson & Jenssen 2002) and for separated wakes over tapered plates (Narasimhamurthy, Andersson & Pettersen 2008). For wing planforms with continuously variable chord length over the wingspan, delta wings have also received substantial attention (Rockwell 1993; Gursul, Gordnier & Visbal 2005; Taira & Colonius 2009). For laminar post-stall flows, wing taper was studied using trapezoidal plates (Huang *et al.* 2015). Nonetheless, there still is a lack of fundamental studies for understanding the role of taper ratio, and how it interplays with leading-edge (LE) and trailing-edge (TE) sweep-angle effects for massively separated laminar flows.

For laminar separated flows, the combined effect of wing taper and sweep remains elusive. In the present work, we aim to reveal the effects of taper in the laminar wake dynamics and the influence of LE and TE sweep angles on the vortical interactions through

a comprehensive campaign of direct numerical simulations of 3-D flows over finite NACA 0015 wings. We characterize the stalled wakes of wings with backward-swept LE and forward-swept TE, identifying the combined effects of taper and sweep on the post-stall wake dynamics. Our work is organized as follows. In § 2, we present our wing planform geometry definitions and the set-up for direct numerical simulations. In § 3, we offer a detailed analysis and classification of the wake structures, highlighting the effects of taper and sweep on the wakes and aerodynamic forces. Finally, we conclude our study by summarizing our findings in § 4.

2. Problem set-up

We consider laminar flows over tapered wings with a NACA 0015 cross-sectional profile. The spatial coordinates of streamwise, transverse and spanwise directions are denoted by (x, y, z), respectively. The origin is placed at the LE of the wing root, as shown in figure 1. The NACA 0015 profile is defined on the (x, y) plane, which is extruded from the wing root in the spanwise direction to form the 3-D wing. Wing taper is defined by the taper ratio $\lambda = c_{tip}/c_{root}$, where c_{tip} and c_{root} are tip and root chord lengths, respectively, as shown in figure 1(*a*). For all wings considered herein, the chord length decreases linearly from root to tip. The non-dimensional mean chord length c at the spanwise location of $z = b/2$ is taken to be the characteristic length used to non-dimensionalize all spatial variables. The mean chord c is fixed and independent of λ for all wing planforms studied herein.

The semi aspect ratio of the wings is set as $sAR = b/c = 1$ and 2, where b is the half-span length, as shown in figure 1(*d*). We consider half-span wing models with symmetry imposed at the root. The angles of attack, $\alpha = 14^\circ$, 18° and 22°, are defined between the airfoil chord line and the streamwise direction. The present wing geometries have sharp TE and straight-cut wing tip. The mean-chord-based Reynolds number is set to $Re_c = 600$ and the free-stream Mach number is set to $M_\infty = 0.1$. Taper changes the local Reynolds number Re_{L_c}, defined as a function of the spanwise location (Traub *et al.* 2015). For the present study, the difference between c_{tip} and c_{root} accounts for a maximum variation of 60 % on Re_{L_c} along the span, from $\min(Re_{L_c}) = 250$ to $\max(Re_{L_c}) = 950$ at the lowest taper ratio.

For tapered swept wings, the 3-D computational set-up is sheared in the chordwise direction and the LE sweep angle is defined between the z direction and the LE. Tapered wings have different LE and TE sweep angles (Λ_{LE} and Λ_{TE}, respectively), as shown in figure 1(*a*). Note that the wing planform can be specified with two parameters out of the three parameters of taper ratio (λ), LE and TE sweep. Given that $(c_{tip} + c_{root})/2 = c$, for a chosen λ, Λ_{LE} and sAR we have

$$\lambda = \frac{c_{tip}}{c_{root}}, \quad \frac{c_{root}}{c} = \frac{2}{1+\lambda} \quad \text{and} \quad \Lambda_{TE} = \arctan\left[-\frac{2}{sAR}\left(\frac{1-\lambda}{1+\lambda}\right) + \tan\left(\Lambda_{LE}\right)\right]. \tag{2.1a–c}$$

In this work, we explore the combined effects of the LE and TE sweep angles on the wake dynamics for LE sweep angles $0 \leq \Lambda_{LE} \leq 50^\circ$ and taper ratios $0.27 \leq \lambda \leq 1$. The corresponding TE sweep angles take $-30^\circ \leq \Lambda_{TE} \leq 50^\circ$. Herein, negative sweep angles indicate a forward sweep, as shown in figure 1(*a*), while a positive sweep angle represents a backward sweep.

Traditionally in aeronautics, tapered swept wings have wing-sweep angles observed with respect to the quarter-chord line (Anderson 1936, 2010; Falkner 1950) denoted by $\Lambda_{c/4}$, as shown in figure 1(*a*). Anderson (1999) considered the half-chord sweep angle $\Lambda_{c/2}$, such

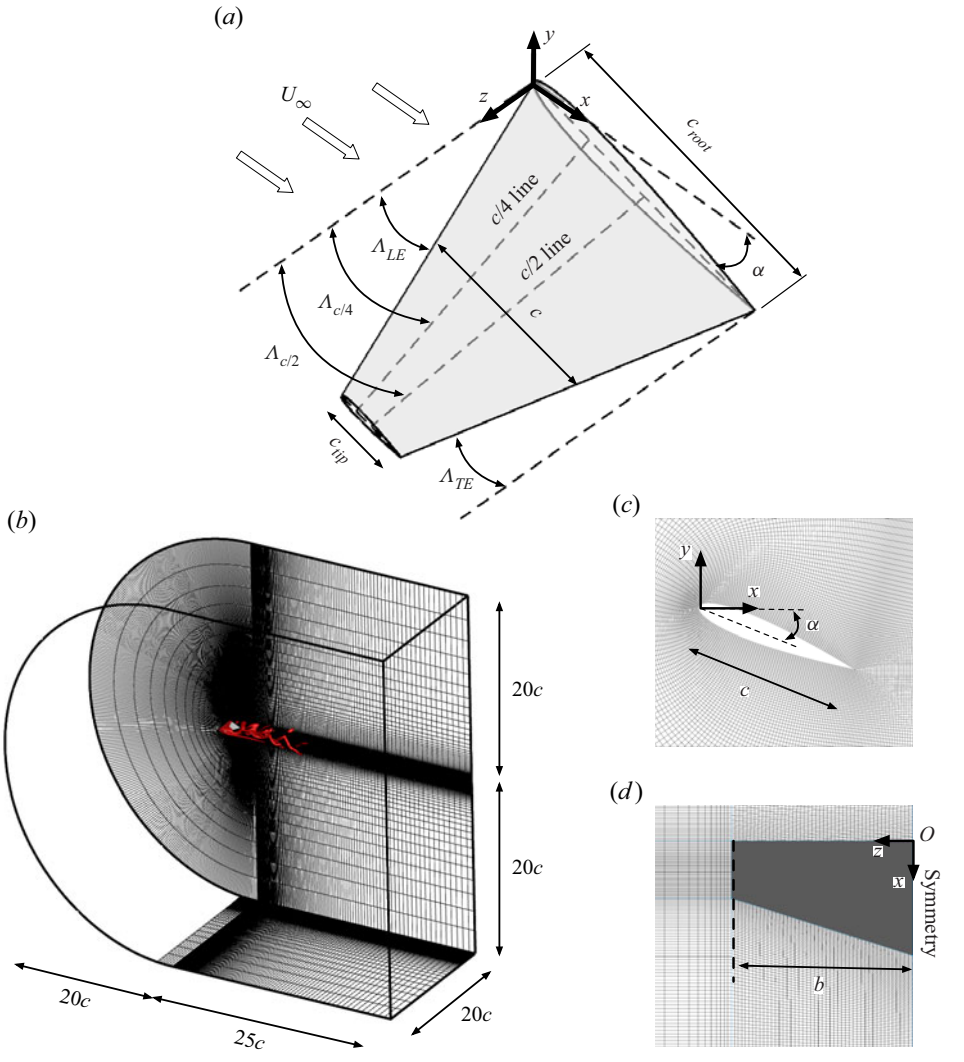

Figure 1. Problem set-up for tapered wings. (*a*) Geometrical parameters shown in a wing planform with $sAR = b/c = 2, \alpha = 18^\circ, \lambda = 0.27$ and $\Lambda_{LE} = 18.4^\circ$. (*b*) For a $(\lambda, \Lambda_{LE}) = (0.5, 0^\circ)$ wing, we show the computational domain and (*c*,*d*) grids with 2-D planes at $z/c = 1$ and $y/c = -0.5$, respectively.

that aerodynamic load distribution becomes independent of the taper ratio. Straight tapered wings with $\Lambda_{c/4} = 0^\circ$ were studied by Traub *et al.* (2015). On the other hand, Irving (1937) considered the effect of the LE and TE sweep angles. For the present laminar post-stall wakes, due to the crucial role played by the LE vortex in defining the wake characteristics (Videler, Stamhuis & Povel 2004; Eldredge & Jones 2019), we focus on the distinct effects of Λ_{LE} and Λ_{TE} in our analysis and describe their influence on the wake dynamics. We note, however, that it is also possible to translate the findings reported herein with respect to the traditional quarter-chord and half-chord sweep angles, $\Lambda_{c/4}$ and $\Lambda_{c/2}$, respectively.

2.1. *Direct numerical simulations*

We conduct direct numerical simulations with a compressible flow solver, *CharLES* (Khalighi *et al.* 2011; Brès *et al.* 2017), which uses a second-order-accurate finite-volume

method in space with a third-order-accurate total-variation diminishing Runge–Kutta scheme for time integration. The computational domain is discretized with a C-type grid with mesh refinement near the wing and in the wake. With the origin at the airfoil LE on the symmetry plane $(x/c, y/c, z/c) = (0, 0, 0)$, the computational domain extends over $(x/c, y/c, z/c) \in [-20, 25] \times [-20, 20] \times [0, 20]$, which yields a maximum blockage ratio of 0.8 % for the wing with $\lambda = 0.27$, $sAR = 2$ and $\alpha = 22^\circ$. The computational set-up is shown in figure 1(*b–d*).

We have prescribed a Dirichlet boundary condition of $(\rho, u_x, u_y, u_z, p) = (\rho_\infty, U_\infty, 0, 0, p_\infty)$ at the inlet and far-field boundaries, where ρ is density, p is pressure and u_x, u_y and u_z are velocity components in x, y and z directions, respectively. The subscript ∞ denotes the free-stream values. A symmetry boundary condition is prescribed along the root plane, $z/c = 0$. We have evaluated the applicability of the root-symmetry boundary condition by conducting direct numerical simulations of flows over full wing configurations, without root symmetry, for wings at $\alpha = 22^\circ$ and $\lambda = 0.27$ and 1. For both wings, we note that the wake exhibits root-concentrated vortex shedding and remains symmetric with respect to the wing root over large computational times.

A no-slip adiabatic boundary condition is set on the airfoil surface. For vortical structures to convect out of the domain, a sponge layer is applied over $x/L_c \in [15, 25]$ with the target state being the running time-averaged state over 5 convective time units (Freund 1997). Simulations start from uniform flow and are performed with a constant acoustic Courant–Friedrichs–Lewy (CFL) number of 1 until transients are washed out of the computational domain. The time to flush out the transients varies depending on the wing planform and angle of attack, generally ranging from 50 to 300 convective time units. After the transients are washed out of the domain, flows are simulated with a constant time step defined such that the CFL number is smaller than one. Flow statistics are collected for 100 to 300 convective time units, depending on the flow-field characteristics and spectral content to ensure convergence. A detailed discussion on verification is provided in Appendix A.

3. Results

3.1. *Overview of tapered wing wakes*

In figure 2, we present instantaneous post-stall flows over tapered wings, which exhibit a rich diversity of wake structures through the combined effects of LE and TE sweep. Taper effects on laminar separated flows are entwined with the effects of LE and TE sweep angles. However, by studying straight tapered wings, that is, wings with $\Lambda_{c/2}$ and $\Lambda_{c/4}$ approximately zero, we can distinguish the effects of taper from other geometrical parameters.

For instance, let us explore the flows over wings with $(\lambda, \Lambda_{LE}) = (1, 0^\circ)$ and compare them with the wake structures around $(\lambda, \Lambda_{LE}) = (0.27, 10^\circ)$ wings; these flows have $\Lambda_{c/4} = 0^\circ$ and 1.8°, respectively. For the tapered wing, we note a significant reduction of the tip vortex length caused by the smaller c_{tip}. The downstream root shedding, however, exhibits similar hairpin-like structures for both wings. In the near-wake region, for the tapered wing, the spatial spanwise flow fluctuations emerge near the root, over the spanwise vortex on the suction side. Such wake oscillations are absent in the vortical structure that forms over the untapered wing.

We can further explore the distinct taper effects on the wake dynamics by considering wings with $\Lambda_{c/2} \approx 0^\circ$, as shown for the similar flow patterns that develop at the root region for $(\lambda, \Lambda_{LE}) = (1, 0^\circ)$ and $(0.27, 18.4^\circ)$ wings. Here, with a lower taper ratio, tip

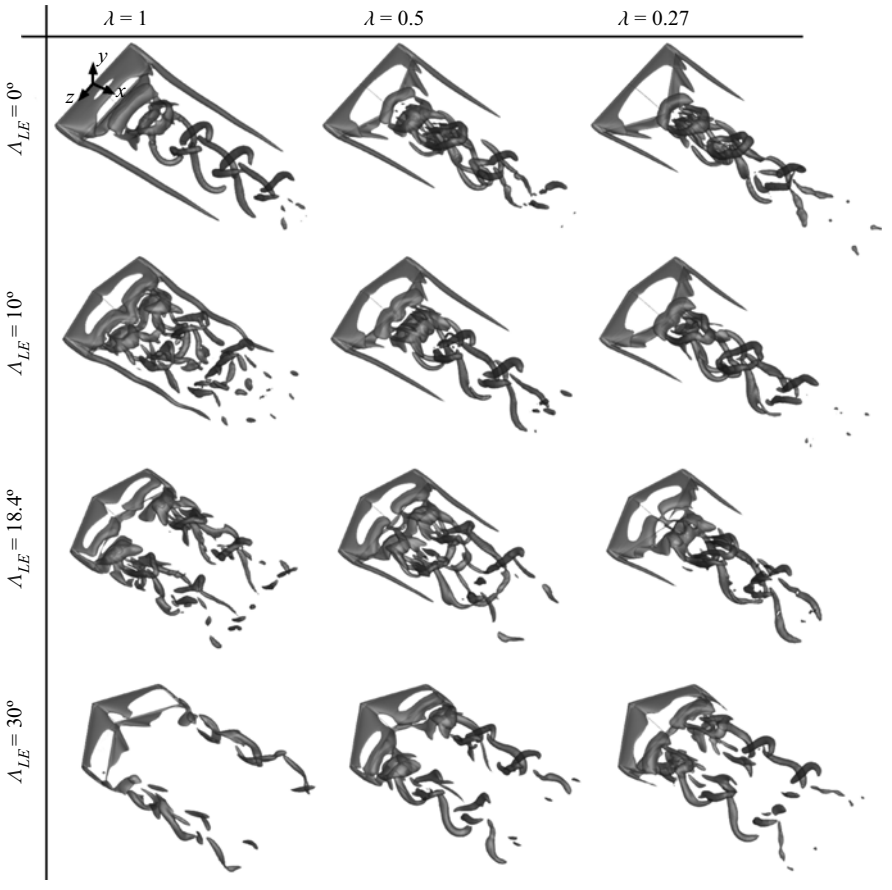

Figure 2. Instantaneous flows around tapered wings with $sAR = 2$, $0.27 \leq \lambda \leq 1$ and $0^\circ \leq \Lambda_{LE} \leq 30^\circ$, at $\alpha = 18^\circ$ visualized using grey-coloured isosurfaces of $Q = 1$.

vortices are considerably weakened when compared with the structures near the free end of the untapered wing. The vortical roll structures emerging over the tapered wing appear slanted and aligned with Λ_{LE}, suggesting that the LE sweep angle plays an important role in defining the behaviour of the near-wake shedding structures.

For tapered wings, the backward-swept LE effect can be observed by fixing $\Lambda_{TE} = 0^\circ$ while the LE is swept backwards with $\Lambda_{LE} = 18.4^\circ$ and 30° for $\lambda = 0.5$ and 0.27, respectively. For such wings, taper shifts the wake-shedding structures closer to the wing tip. An opposite effect is shown in the top row of figure 2, for flows over forward-swept TE wings. These planforms have fixed $\Lambda_{LE} = 0^\circ$, while $\Lambda_{TE} = -18.4^\circ$ and -30° for $\lambda = 0.5$ and 0.27, respectively. For these cases, we observe that taper reduces the tip vortex length and changes the topology of the root shedding structures. Let us further study the taper effect for highly swept wings, shown in the bottom row of figure 2, with fixed $\Lambda_{LE} = 30^\circ$, while $\Lambda_{TE} = 13.7^\circ$ and 0° for $\lambda = 0.5$ and 0.27, respectively. Here, taper increases the amplitude of wake oscillations. We further detail the discussions of the effects of taper, LE and TE sweep in § 3.3.

The variety of wake structures that appear around tapered wings, as seen in figure 2, calls for a proper characterization of the wake dynamics that associates its behaviour with the wing planform geometry. The above discussions suggest that taper affects the

location where unsteadiness emerges and the characteristics of the vortical structures. In the following section, we provide a map that characterizes the wakes of tapered wings.

3.2. *Wake classification and aerodynamic forces*

We now classify the flow patterns with respect to the wing geometry. Our criterion is based on the examination of the flow characteristics downstream of the airfoil on a 2-D plane at $x/c = 4$, where we identify the spatial location of maximum time-averaged $\bar{Q}$ and the maximum fluctuating component of $Q' = Q - \bar{Q}$, where Q is the second invariant of the velocity gradient tensor used to identify the vortical structures (Hunt, Wray & Moin 1988; Jeong & Hussain 1995). Maximum $\bar{Q}$ and Q' located between $0 \leq z/(c\ sAR) < 0.5$ are labelled root-dominant, while points with maximum $\bar{Q}$ or Q' between $0.5 \leq z/(c\ sAR) \leq 1$ are named tip-dominant. We consider the flow as steady when the maximum fluctuating value of Q' is smaller than 0.1 at $x/c = 4$. Using the root and tip locations of $\bar{Q}$ and Q', we classify their wakes into three unsteady and two steady regimes, as shown in figure 3, where the steady–unsteady threshold (black dotted line) is computed via biharmonic spline interpolation. We further verify our classification criterion by carefully inspecting the flow fields. Instantaneous flow fields for all tapered wings shown in figure 3 are provided in Appendix B using isosurfaces of $Q = 1$ coloured by streamwise velocity u_x.

The first flow regime ($\blacktriangle$) is composed of tapered wing wakes that have both maximum $\bar{Q}$ and Q' found near the root region. Such wakes appear for tapered wings with low LE sweep angles. For such wings, the tip vortex tends to be short in length and the taper and forward-swept TE effects concentrate shedding at the wing root, as shown in figure 3(*a*) for $(\lambda, \Lambda_{LE}) = (0.27, 20^\circ)$ at $\alpha = 22^\circ$. The second flow regime of unsteady wakes ($\blacklozenge$) occurs when both maximum $\bar{Q}$ and Q' are found over the tip region. Such wakes are observed around tapered wings over a broad range of λ values, being present for wings with high LE sweep angles. The flow over such wings often exhibits hairpin-like vortices downstream in the wake aligned with the wing tip, as shown in figure 3(*b*) for $(\lambda, \Lambda_{LE}) = (0.27, 50^\circ)$ at $\alpha = 22^\circ$.

The third flow regime of unsteady wakes ($\blacktriangleleft$) around tapered wings presents maximum $\bar{Q}$ at the wing tip with maximum Q' at the root. This wake characteristic is often present for slightly tapered and swept wings, that is, wings with high λ and low LE sweep angles. Such wings exhibit a distinct tip vortex formation, at the location of the maximum $\bar{Q}$, and wake shedding near the root. On some occasions, the tip vortex exhibits weak unsteady flow oscillations, as shown in figure 3(*c*) for $(\lambda, \Lambda_{LE}) = (1, 10^\circ)$ at $\alpha = 22^\circ$, while the most energetic vortices are generally observed over the root region.

There are two distinct flow regimes of steady wakes shown herein, as seen in figure 3(*d*,*e*). The first one ($\triangledown$) is comprised of wakes with a steady streamwise vortex that develops into the wake. Such flows are mainly exhibited around highly swept $sAR = 2$ wings with high and moderate taper ratios, $\lambda \geq 0.5$, as shown in figure 3(*d*) for $(\lambda, \Lambda_{LE}) = (0.5, 50^\circ)$ at $\alpha = 22^\circ$. The second steady wakes regime ($\square$) is comprised of flows with no significant wake structures, with maximum $\bar{Q} \leq 0.1$ in the wake and are commonly observed for $sAR = 1$ wings, as shown in figure 3(*e*) for a $(\lambda, \Lambda_{LE}) = (1, 30^\circ)$ wing at $\alpha = 14^\circ$, and for $sAR = 2$ wings at lower angles of attack, low taper ratios and high LE sweep angles.

In figure 3(*f*–*k*), we present the classification for all wings studied herein. For $sAR = 1$ wings, whose classification is shown in figure 3(*f*–*h*), there are fewer changes in wake class, when compared with $sAR = 2$ wings. For the higher-aspect-ratio wings, with a fixed Λ_{LE}, we often notice two or three distinct classes of wake behaviour as λ changes. On the

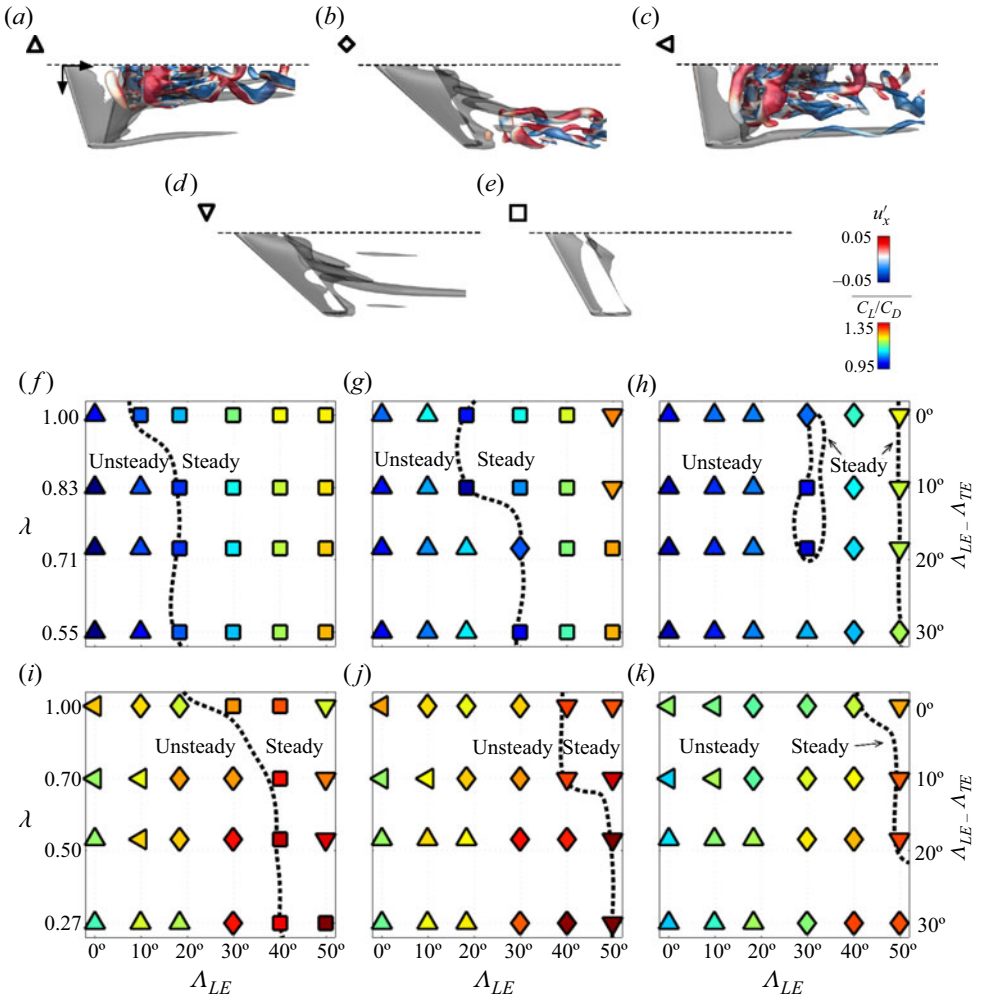

Figure 3. Classification of laminar flows over tapered wings into five distinct wake patterns (*a–e*) shown for $sAR = 2$ wings visualized with time-averaged $\bar{Q} = 1$ in grey and instantaneous $Q' = 0.2$ coloured by u'_x. Classification map for (*f–h*) $sAR = 1$ and (*i–k*) $sAR = 2$ coloured by $\overline{C_L/C_D}$. Black dashed lines mark transition from steady to unsteady flows. (*a*) $(\lambda, \Lambda_{LE}, \alpha) = (0.27, 20^\circ, 22^\circ)$, (*b*) $(\lambda, \Lambda_{LE}, \alpha) = (0.27, 50^\circ, 22^\circ)$, (*c*) $(\lambda, \Lambda_{LE}, \alpha) = (1, 10^\circ, 22^\circ)$, (*d*) $(\lambda, \Lambda_{LE}, \alpha) = (0.5, 50^\circ, 22^\circ)$, (*e*) $(\lambda, \Lambda_{LE}, \alpha) = (1, 30^\circ, 14^\circ)$, (*f*) $sAR = 1, \alpha = 14^\circ$, (*g*) $sAR = 1, \alpha = 18^\circ$, (*h*) $sAR = 1, \alpha = 22^\circ$, (*i*) $sAR = 2, \alpha = 14^\circ$, (*j*) $sAR = 2, \alpha = 18^\circ$ and (*k*) $sAR = 2, \alpha = 22^\circ$.

other hand, for $sAR = 1$ wings, the same class for all λ is observed regularly. Taper effects become increasingly important for $sAR = 2$ wings to alter their wake characteristics, as shown in figure 3(*i–k*), not only affecting the steady–unsteady wake behaviour, but also producing distinct wakes as a function of λ. For $sAR = 2$ wings with high LE sweep angles, the transition from steady to unsteady wakes is dependent on λ. Generally, untapered wings with high LE sweep angle wakes remain steady, while unsteady flow structures emerge in the wakes of tapered swept wings.

The combination LE sweep angle increase and taper ratio decrease is shown to promote wake unsteadiness. In addition, tapered wings with high LE sweep angles exhibit enhanced aerodynamic performance when compared with untapered and unswept wings, as shown in figure 3(*f–k*). To visualize this trend, each symbol associated with a wake class is coloured

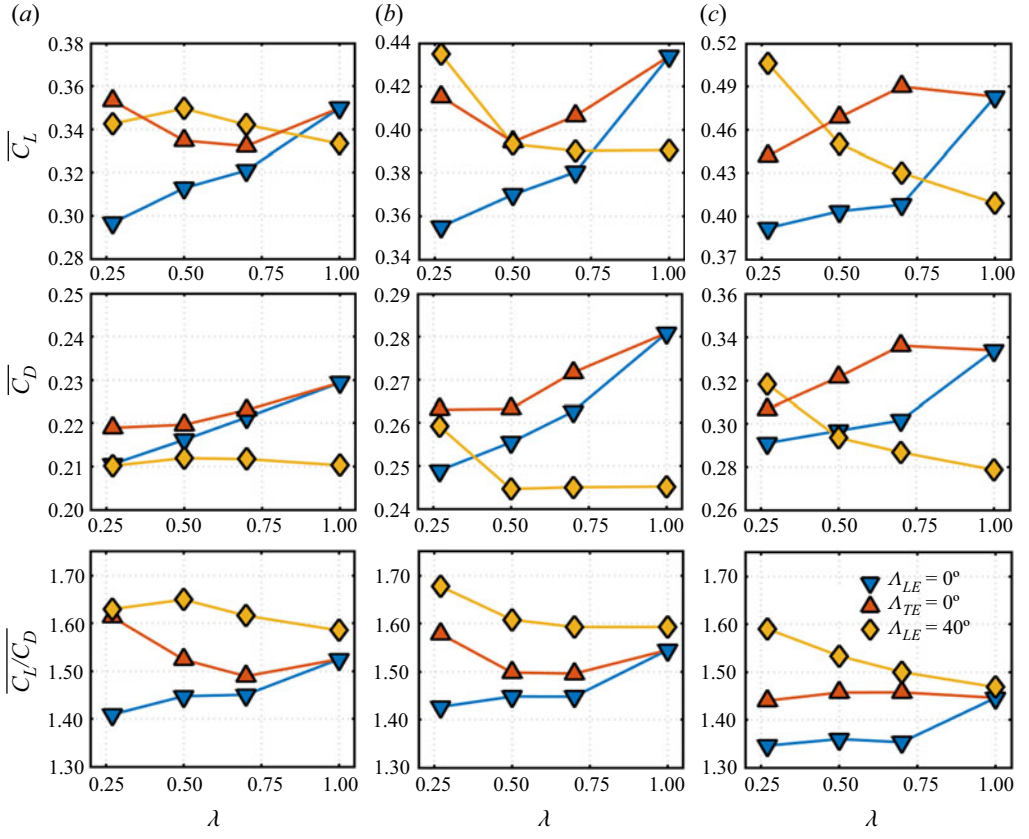

Figure 4. Time-averaged lift, drag and lift-to-drag coefficients, $\overline{C_L}$, $\overline{C_D}$ and $\overline{C_D}$, respectively, for $sAR = 2$ tapered wings with $0.27 \leq \lambda \leq 1$ at (*a–c*) $14° \leq \alpha \leq 22°$. Blue downward-pointing triangles, wings with unswept LE and forward-swept TE; red upward-pointing triangles, wings with backward-swept LE and unswept TE; yellow diamonds, wings with $\Lambda_{LE} = 40°$. (*a*) $\alpha = 14°$, (*b*) $\alpha = 18°$ and (*c*) $\alpha = 22°$.

by the time-averaged lift-to-drag ratio, $\overline{C_L/C_D}$, showing that the higher lift-to-drag ratio coefficients, for all sAR and α combination, appear for the wings with lower λ and higher backward-swept LE. Here, the aerodynamic forces are reported with lift and drag coefficients defined as

$$C_L = \frac{F_y}{\frac{1}{2}\rho U_\infty^2 bc} \quad \text{and} \quad C_D = \frac{F_x}{\frac{1}{2}\rho U_\infty^2 bc}, \tag{3.1a,b}$$

where F_x and F_y are the x and y components of the force on the wing, respectively. Furthermore, we study the aerodynamic loads through the time-averaged $\overline{C_L}$, $\overline{C_D}$ and $\overline{C_L/C_D}$ for selected $sAR = 2$ wings, as shown in figure 4, to reveal the influence of taper and sweep on the aerodynamic forces. The blue symbols present the aerodynamic loads for tapered wings with unswept LE and forward-swept TE. The red symbols show the results for tapered wings with backward-swept LE and unswept TE, while the yellow symbols represent tapered wings with $\Lambda_{LE} = 40°$.

The effects of wing taper on the wakes and aerodynamic forces are strongly dependent on the combination of taper and sweep angle. Let us start from the untapered and unswept wings, marked by blue downward-pointing triangles at $\lambda = 1$. The flow fields around these wings are characterized by root shedding and a strong tip vortex, as seen in figure 2.

While keeping the LE unswept, the TE is forward-swept for low λ. In the wake, such taper produces a concentration of both steady and fluctuating wake structures near the root, as shown in figure 3(*i–k*). A root-concentrated wake with a small tip vortex substantially decreases $\overline{C_L}$, $\overline{C_D}$ and $\overline{C_L/C_D}$ with λ. It is noteworthy that at the same λ, tapered wings having backward-swept LE and unswept TE exhibit a higher $\overline{C_L}$ and $\overline{C_L/C_D}$, as shown in figure 4. For such wings, we recall that taper shifts wake structures towards the tip region, as shown in figure 2.

Backward-swept LE enhances the aerodynamic efficiency of tapered wings in post-stall laminar flow conditions. This LE-sweep-induced improvement in aerodynamic loads also occurs for tapered wings with high LE sweep angles. For instance, untapered swept wings present lower values of $\overline{C_L}$ for all angles of attack, as shown by the diamond-shaped yellow symbols for $\lambda = 1$ in figure 4, while significantly reducing wake oscillations, as shown in figures 2 and 3(*d–f*).

For $sAR = 2$ wings with high LE sweep at high incidence $\alpha \geq 18^\circ$, taper causes a change in the wake regime, as shown in figure 3(*i–k*). For such wings, wake shedding emerges near the wing tip. The change in wake flow regime for tapered wings at high incidence causes an increase in $\overline{C_L/C_D}$. At lower incidence, $\alpha = 14^\circ$, the wake regime remains steady without noticeable vortices for tapered wings and the aerodynamic forces remain fairly constant for all λ, as shown in figure 4(*a*). Let us now describe in detail the taper effects on the wake characteristics in the following section and relate the wakes to the lift distribution over the wing.

3.3. *Wake characteristics*

3.3.1. *Tapered wings with unswept LE and forward-swept TE*

Let us take a closer look at the effect of wing taper for unswept LE wings with forward-swept TE, as it allows us to isolate the Λ_{TE} effect on the wake dynamics. For tapered wings with $\lambda = 0.27, 0.5, 0.7$ and 1, the planforms we study in this section have $\Lambda_{TE} = -30^\circ, -18.4^\circ, -10^\circ$ and 0°, respectively. The negative Λ_{TE} indicates forward sweep. The LE is fixed with $\Lambda_{LE} = 0^\circ$. For such wings, taper has a negative impact on the aerodynamic performance, while concentrating the unsteady shedding to a narrow region near the root, and significantly reducing the tip vortex strength, as shown in figure 5(*a*).

Tapered wings have a smaller c_{tip}, which weakens the tip vortices and decreases their length, alleviating the inboard downwash over the wing. Such tip vortex attenuation and the aforementioned concentration of shedding over the root region occur for all angles of attack shown herein. The influence of the incidence angle appears on the formation of secondary vortices near the wing tip. For wings at high incidence angle, a secondary tip vortex is known to emerge from the LE, as shown in figure 6 (DeVoria & Mohseni 2017; Zhang *et al.* 2020*b*). For the tapered wings with forward-swept TE at $\alpha = 22^\circ$, there is also another core vortex that emerges near the wing tip from the TE. This structure is seen over the vortex sheet rolling up the TE as a slanted vortex pointing towards the root for the lower taper ratio, as visualized in figure 6.

To gain further insights into the characteristics of wake vortices, we study the unsteady flow behaviour over the wingspan using probe measurements of velocity fluctuations over $x/c \in [3, 4]$, $y/c \in [-1.5, 0.5]$. The x/c location is arbitrary and does not affect significantly the results. The y/c range encompasses the region where vortical structures appear. Over this region, we probe the norm of the root mean square of the velocity, $\|\boldsymbol{u}'\|_2$. This measurement represents the spanwise distribution of flow unsteadiness, as shown in figure 5(*b*).

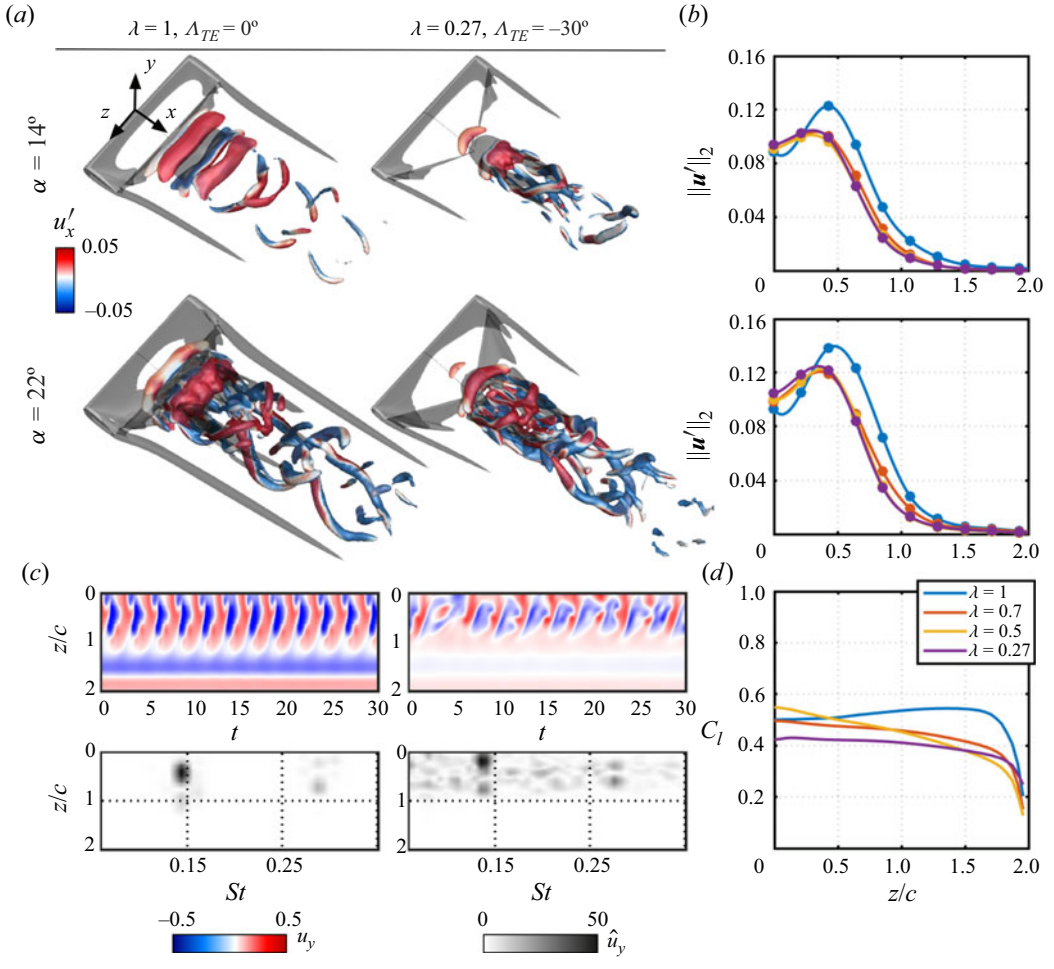

Figure 5. (*a*) Isosurfaces of flow fields around tapered wings with $sAR = 2$, $\Lambda_{LE} = 0°$, $\lambda = 0.27$ and 1, $\alpha = 14°$ and 22°. Time-averaged $\bar{Q} = 1$ isosurface is shown in grey. Instantaneous $Q' = 0.2$ isosurface is shown coloured by u'_x. (*b*) Spanwise distribution of $\|\boldsymbol{u}'\|_2$ for different λ for $\Lambda_{LE} = 0°$ wings. (*c*) Spatial–temporal (top) and PSD (bottom) of u_y distribution over the spanwise direction from probes located at $(x, y)/c = (3, -0.5)$ for the $\lambda = 0.27$ and 1 tapered wings at $\alpha = 22°$ shown above. (*d*) Sectional lift distribution over wingspan for tapered wings at $\alpha = 22°$.

By examining at the spanwise $\|\boldsymbol{u}'\|_2$ distribution in figure 5(*b*) for untapered wings (blue), we notice that the flow unsteadiness peaks at $z/c \approx 0.5$ and decays towards the wing tip for both angles of attack. For tapered wings, the spanwise $\|\boldsymbol{u}'\|_2$ curves are independent of the taper ratio for $\lambda \leq 0.7$. For such wings, taper yields an attenuation of the $\|\boldsymbol{u}'\|_2$ peak. The peak of $\|\boldsymbol{u}'\|_2$ also moves towards $z/c \approx 0$, showing a concentration of unsteadiness towards the wing root for tapered wings.

Next, we analyse the spatial–temporal distribution of u_y from probes located at $(x, y)/c = (3, -0.5)$ over the spanwise direction, to investigate how wing taper affects the shedding behaviour. Herein, temporal frequency is characterized through the Strouhal number defined as $St = f(c \sin\alpha/U_\infty)$, where f is the frequency. For comparison, the wake spectrum for the flow over an untapered wing is shown on the left of figure 5(*c*). For this wing, there is a narrow peak of oscillations at $St \approx 0.14$. The wake spectrum is clean with a

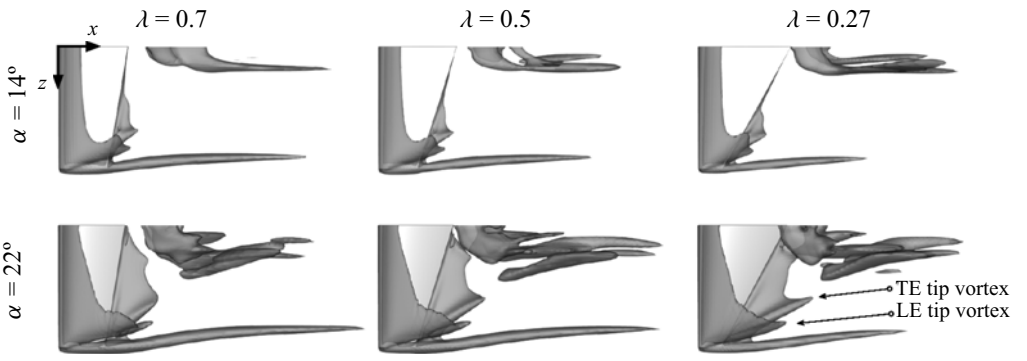

Figure 6. Vortical structures emerging near the wing tip around tapered wings with unswept LE and forward-swept TE. Top view of time-averaged flow fields around $sAR = 2$ tapered wings at $\alpha = 14^\circ$ and 22°, with $\Lambda_{LE} = 0^\circ$, visualized using grey-coloured time-averaged isosurfaces of $\bar{Q} = 2$.

vortex-shedding pattern comprised of spanwise-dominated vorticity near the root, forming hairpin vortices and a steady streamwise vortex at the wing tip. For the tapered wing, the spectrum is broadband as a result of the mixing of streamwise and spanwise vortices near the wing root. Even though the wake exhibits more mixing, the spanwise structures remain dominant, being related to the power spectral density (PSD) peak at $St \approx 0.13$. We note that the PSD peak occurs at a lower St than that observed for the untapered wing, as the core unsteady structures that populate the downstream wake arise from the root region of the wing, where the chord length is large.

As the post-stall wakes around tapered wings with forward-swept TE concentrate shedding near the root, they also alter the sectional load distribution as the near-wake vortices play an important role in generating lift and drag over the wing. While untapered wings exhibit a peak in sectional lift near the tip region, we note that the root contribution to lift is higher for tapered wings, as shown in figure 5(d). Such load distribution is generally positive for flight stability (Anderson 2010). For laminar post-stall flows over wings, the emergence of near-wake vortices closer to the wing surface can provide added lift (Lee *et al.* 2012; Zhang & Taira 2022). As shown in figure 5(a), there are fewer large near-wake structures over the wing for the lower λ. This is a possible reason of the decrease in C_l over the entire wingspan experienced by the $\lambda = 0.27$ wing.

3.3.2. *Tapered wings with backward-swept LE and unswept TE*

Next, let us analyse the taper effects of wings with backward-swept LE and fixed unswept TE, to understand and separate the effects of Λ_{LE} on the global wake. For such wings with $\lambda = 0.27, 0.5, 0.7$ and 1, the planforms have $\Lambda_{LE} = 30^\circ, 18.4^\circ, 10^\circ$ and 0°, respectively. The positive Λ_{LE} indicates backward sweep. The TE is fixed with $\Lambda_{TE} = 0^\circ$. For such wings, taper yields an opposite effect on the wake characteristics, when compared with those discussed in § 3.3.1. As shown in figure 4, such wake pattern results in a better aerodynamic performance for wings with the same λ but distinct LE and TE sweep angles. Herein, taper shifts the unsteadiness region towards the wing tip, as shown in figure 7(a).

Concurrently, the tip vortex weakens for tapered wings with the shortened c_{tip}, which alleviates the inboard downwash near the tip, similar to what was observed for the wings in § 3.3.1. This increases the effective angle of attack near the tip and allows for the flow to detach from the wing surface and form wake-shedding structures near $z/c \approx 1$, as shown in figure 7(a). We quantify the effect of wing taper on flow unsteadiness through

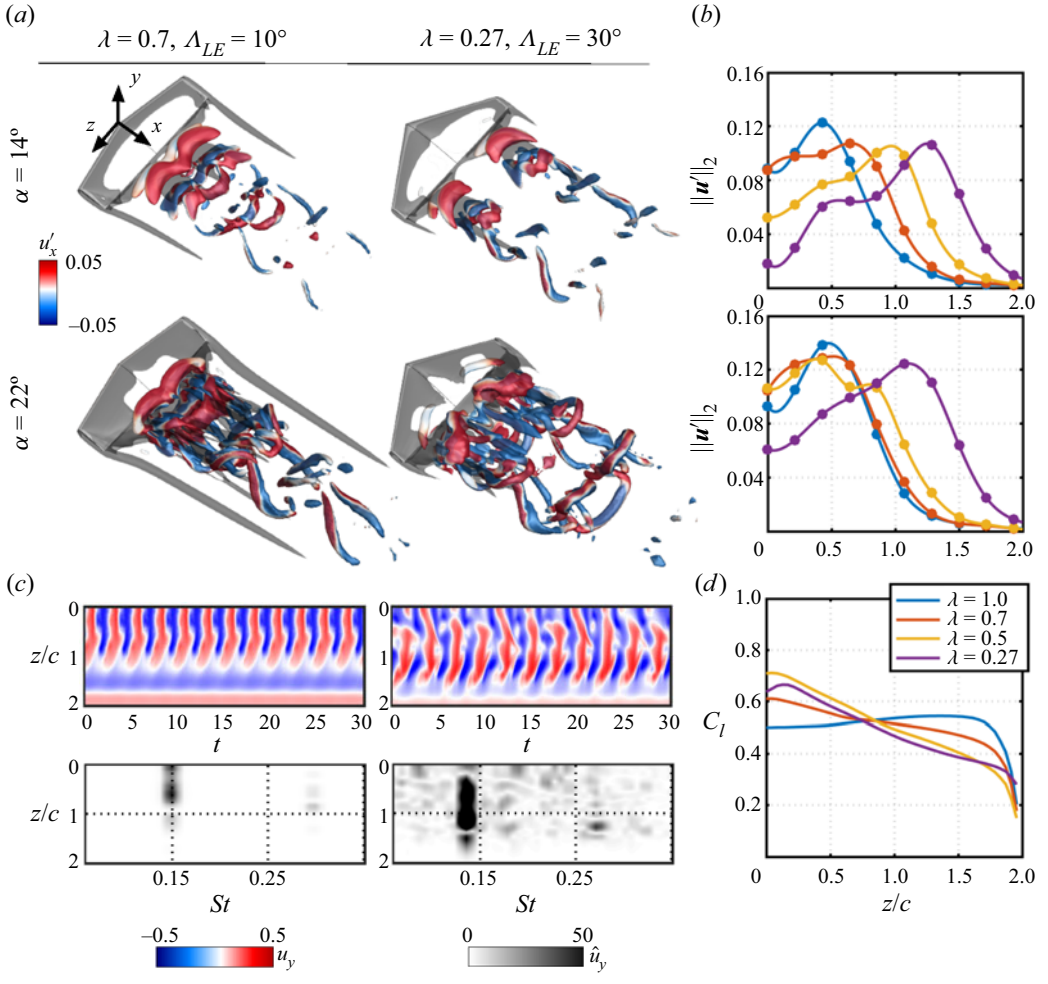

Figure 7. (*a*) Isosurfaces of flow fields around tapered wings with $sAR = 2$, $\Lambda_{TE} = 0°$, $\lambda = 0.27$ and 0.7, $\alpha = 14°$ and $22°$. Time-averaged $\bar{Q} = 1$ isosurface is shown in grey. Instantaneous $Q' = 0.2$ isosurface is shown coloured by u'_x. (*b*) Spanwise distribution of $\|\boldsymbol{u}'\|_2$ for different λ for $\Lambda_{LE} = 0°$ wings. (*c*) Spatial–temporal (top) and PSD (bottom) of u_y distribution over the spanwise direction from probes located at $(x, y)/c = (3, -0.5)$ for the $\lambda = 0.27$ and 0.7 tapered wings at $\alpha = 22°$ shown above. (*d*) Sectional lift distribution over wingspan for tapered wings at $\alpha = 22°$.

the winsgpan distribution of $\|\boldsymbol{u}'\|_2$, as shown in figure 7(*b*). For both angles of attack, taper affects the wake-shedding distribution over the wingspan. For $\lambda = 0.27$ (purple), at $\alpha = 22°$, the peak of $\|\boldsymbol{u}'\|_2$ appears near the quarter-span at $z/c \approx 1.25$, with a gradual transition towards $z/c \approx 0.5$ from $\lambda = 0.27$ to 1.

As seen in figure 7(*b*), tapered wings with backward-swept LE and unswept TE exhibit unsteadiness over a larger spanwise length than untapered wings. For instance, let us observe the spanwise $\|\boldsymbol{u}'\|_2$ distribution for wings at $\alpha = 22°$. For the untapered wing (blue), $\boldsymbol{u}' \geq 0.02$ over $0 \leq z/c \leq 1$, which is the region where significant unsteady wake structures appear. Now, for the tapered wing with $\lambda = 0.27$, $\boldsymbol{u}' \geq 0.02$ over $0 \leq z/c \leq 1.6$, hence large unsteady structures can be observed over a larger spanwise portion of the wake.

The spatial–temporal distribution of the transverse velocity u_y over the spanwise direction also shows that the wake of backward-swept LE and unswept TE tapered wings

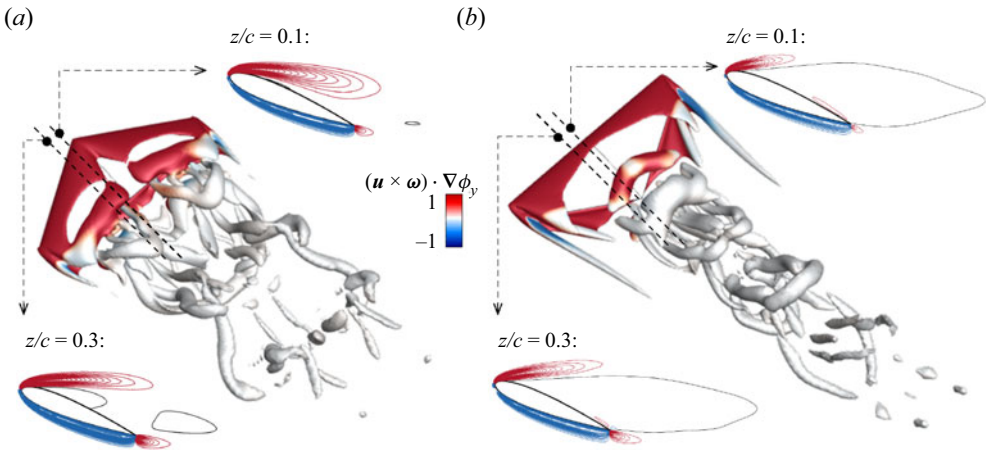

Figure 8. Lift elements around $\lambda = 0.27$ tapered wings at $\alpha = 22^\circ$ at the time of maximum lift. (a) Backward-swept LE with unswept TE and (b) unswept LE with forward-swept TE . Perspective view shown with isosurfaces of $Q = 1$ coloured by $(\boldsymbol{u} \times \boldsymbol{\omega}) \cdot \nabla\phi_y$. Slices at selected z/c locations with isocontours of lift elements and a black solid line over $\overline{u_x} = 0$.

exhibits 3-D vortical structures that result in a broadband wake spectrum, as shown in figure 7(c). The wake, however, is mainly dominated by large quasi-2-D spanwise aligned vortex rolls observed for all taper ratios. For $\lambda = 0.27$, as unsteadiness appears over a larger portion of the wingspan, the stronger shedding structures are hairpin-like vortices that appear between $0.5 \leq z/c \leq 1.5$, as shown on the right of figure 7(c).

The sectional lift distribution, shown in figure 7(d), reveal that tapered wings with backward-swept LE and unswept TE significantly increase the root contribution and reduce the influence of the near-tip region on the overall lift. The increase in root contribution to lift results from the shifting of the separation bubble towards the tip. This shifting causes a pair of near-wake vortices to emerge over the wing surface at the root region, as shown in figure 7(a). Using force element analysis (Chang 1992), we reveal the near-wake structures that contribute to lift. In this approach, the volume force elements are identified by the dot product of the Lamb vector $\boldsymbol{u} \times \boldsymbol{\omega}$ and an auxiliary potential $\nabla\phi_i$ (details in Appendix C). Force element analysis shows a vortex pair emerging near the root, which increases the local contribution to the total lift over the wing.

In figure 8, force elements further show that vortical structures with major contribution to lift appear over the separation bubble. Here, this region is illustrated by a black solid line contour at $\overline{u_x} = 0$ on the 2-D slices at $z/c = 0.1$ and 0.3. In particular, the emergence of the near-root vortex pair is persistent for wings with backward-swept LE as similar structures have been identified for backward-swept untapered wings by Zhang & Taira (2022). These structures are absent for unswept LE wings, both tapered and untapered, as shown in figure 8(b). In fact, force elements over tapered unswept LE wings show that the lift elements emerging over the wing are much smaller than those over tapered wings with backward-swept LE. As the separation bubble near the root becomes larger over tapered wings with unswept LE, the wake structures are shifted far from the wing, reducing their contribution to the total lift.

The tip vortex is also substantially affected by wing taper, becoming smaller than the tip vortex around untapered wings, as shown in figure 9(a). Tip vortices have high importance in terms of the aerodynamic characteristics of the wing (Francis & Kennedy 1979; Green & Acosta 1991; Devenport *et al.* 1996; Birch *et al.* 2004; Taira & Colonius 2009; Dong *et al.* 2020; Zhang *et al.* 2020*b*; Toppings & Yarusevych 2021, 2022) and, in the case of tapered

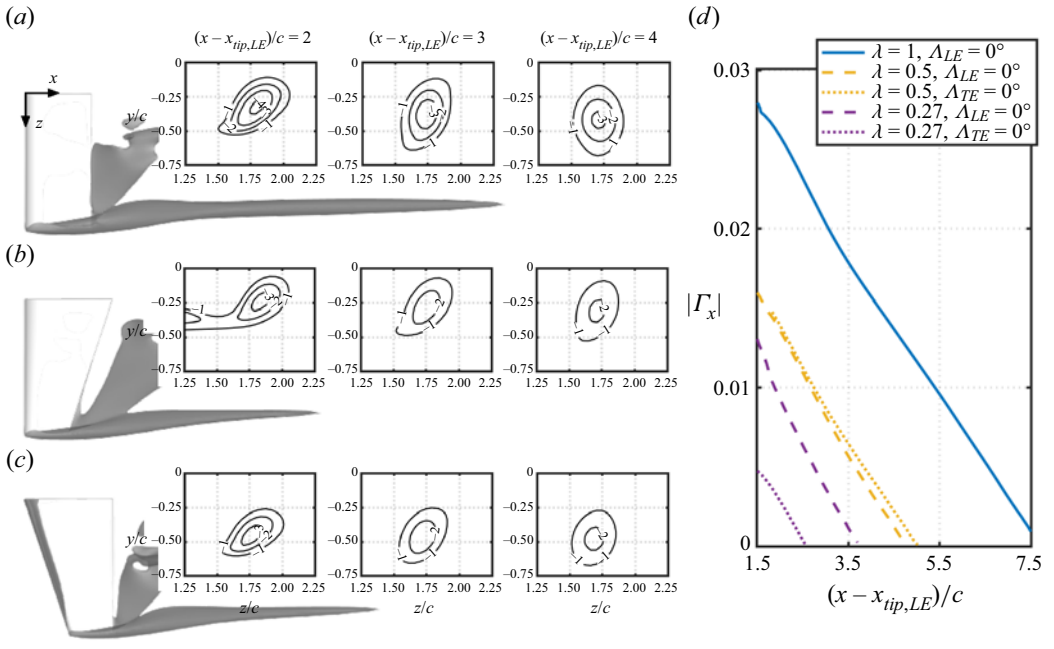

Figure 9. Streamwise circulation $|\Gamma_x|$ of tip vortex around (*a*) an untapered wing and tapered wings with $\lambda = 0.5$ with (*b*) unswept LE and forward-swept TE and (*c*) backward-swept LE and unswept LE at $\alpha = 22°$. Flow field visualized with grey-coloured isosurfaces of $\bar{\omega}_x = -2$ and 2-D slices with isolines of $\bar{\omega}_x$ at specific $(x - x_{tip,LE})/c$ locations. The magnitude of $|\Gamma_x|$ computed for the isocontour of (*d*) $\overline{\omega_x} = -2$ for tapered swept wings with different planform configurations.

wings, due to the small c_{tip}, tip vortices are attenuated, as a result of the reduced pressure differences between upper and lower sides of the wing near the tip. Beyond that, even for wings with the same λ, the tip vortex behaviour can be shifted in the x direction depending on how the wing is tapered, whether it has a backward-swept LE or a forward-swept TE, as shown in figure 9(*b*,*c*). For this reason, we must also analyse the tip vortex at a distance x/c from the LE at the wing tip, which is identified herein as $x_{tip,LE}$.

We can observe how wing taper affects the strength of the tip vortex by analysing $\overline{\omega_x}$ near the tip, as shown in figure 9(*a–c*). The isosurfaces of $\overline{\omega_x}$ and the contour lines at representative $(x - x_{tip,LE})/c$ locations show the decay of vorticity magnitude for tapered wings with $\lambda = 0.5$. However, the effect of taper is not the same for both wings, even though they share the same taper ratio. This difference can be quantified as we compute the streamwise circulation $\Gamma = \int_C = \boldsymbol{u} \cdot \mathrm{d}\boldsymbol{l}$. Here, C is the isocontour of $\overline{\omega_x} = -2$, as shown in figure 9(*d*). The choice of $\overline{\omega_x}$ level is carefully chosen to isolate the tip vortex.

The tip vortex diffuses downstream of the wing, which makes the $|\Gamma_x|$ profiles decay slowly (Edstrand *et al.* 2018; Zhang *et al.* 2020*b*). In general, for tapered wings the reduction in c_{tip} is the main cause of the tip vortex weakening; thus the $|\Gamma_x|$ circulation decays with λ at any distance from the wing tip. The circulation $|\Gamma_x|$ further reveals how different types of wing taper can affect the strength of the tip vortex, as shown in figure 9(*d*). At any given streamwise distance from the wing tip at the LE, $(x - x_{tip,LE})/c$, for $\lambda = 0.5$, the streamwise circulation decay is similar for both tapered wings. For $\lambda = 0.27$, the tip vortex strength decays considerably depending on the LE and TE sweep angles. For tapered wings with backward-swept LE and unswept TE, the root shedding is shifted towards the tip region and reduces the tip vortex strength at any distance from the TE, when compared with the wing with same λ and forward-swept TE. For forward-swept

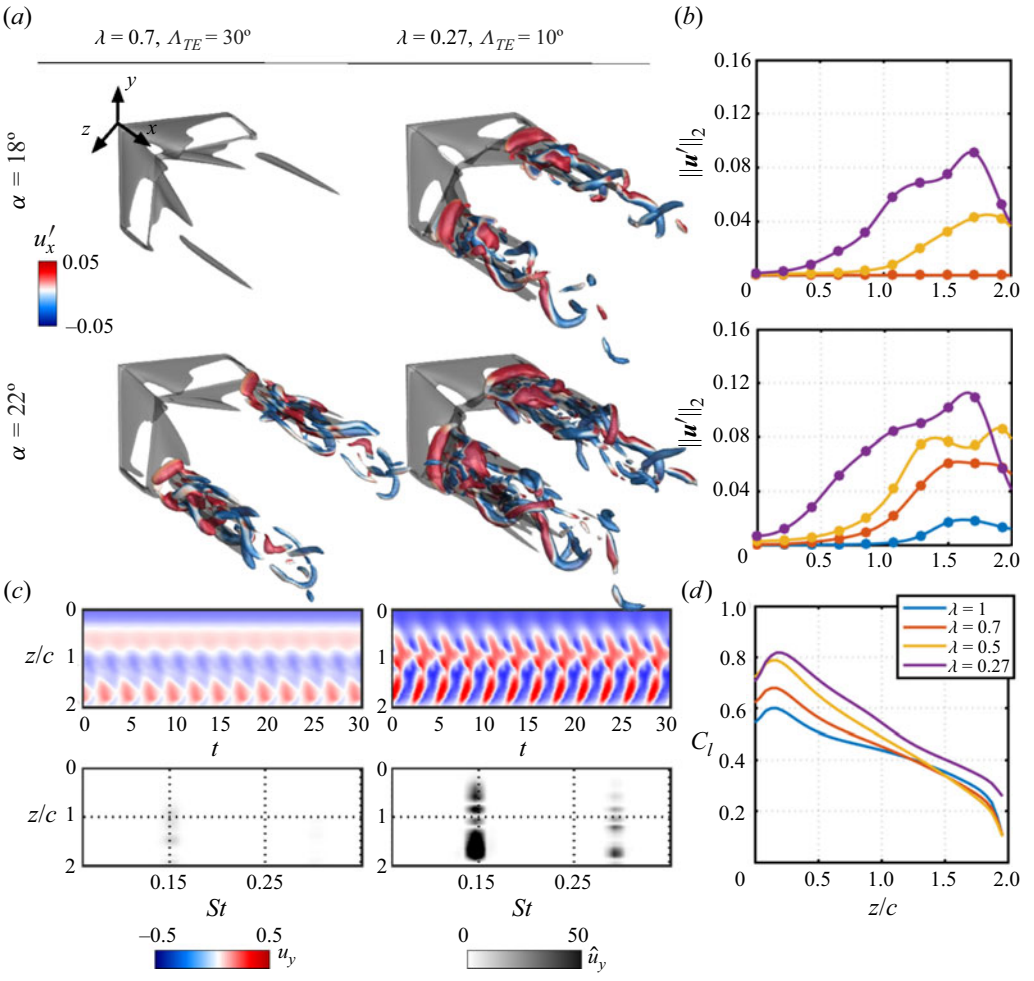

Figure 10. (*a*) Isosurfaces of flow fields around tapered swept wings with $sAR = 2$, $\Lambda_{LE} = 40°$, $\lambda = 0.27$ and 0.7, $\alpha = 18°$ and 22°. Time-averaged $\bar{Q} = 1$ isosurface is shown in grey. Instantaneous $Q' = 0.2$ isosurface is shown coloured by u'_x. (*b*) Spanwise distribution of $\|\boldsymbol{u}'\|_2$ for different λ for $\Lambda_{LE} = 0°$ wings. (*c*) Spatial–temporal (top) and PSD (bottom) of u_y distribution over the spanwise direction from probes located at $(x, y)/c = (3, -0.5)$ for the $\lambda = 0.27$ and 0.7 tapered wings at $\alpha = 22°$ shown above. (*d*) Sectional lift distribution over wingspan for tapered wings at $\alpha = 22°$.

TE wings, as vortex shedding is concentrated near the wing root, it has a minor influence on the tip vortex.

3.3.3. *Tapered wings with high LE sweep angles*

The final class of tapered wing shapes we consider are those with high LE sweep. For the swept wings discussed herein, with $\Lambda_{LE} > 30°$, wake oscillations are strongly attenuated. For laminar flows over untapered wings with high sweep angles at moderate angles of attack, the wake becomes steady, while at high angles of attack, unsteadiness may develop in the wing tip region (Zhang *et al.* 2020*a*; Ribeiro *et al.* 2023*b*). For highly swept and tapered wings, the flow exhibits wake shedding for small λ, as shown in figure 10(*a*).

Here, we analyse wings with a fixed $\Lambda_{LE} = 40^\circ$, while the TE is swept with $\Lambda_{TE} = 10^\circ, 21.6^\circ, 30^\circ$ and 40° for $\lambda = 0.27, 0.5, 0.7$ and 1, respectively. The onset of shedding for highly swept and tapered wings results from the distinct effects of Λ_{LE} and Λ_{TE}. For the present tapered swept wings, the vortical structures emerging from the TE promote unsteadiness in the wake near the wing tip. For lower taper ratios, wings have a low Λ_{TE}, which causes wake oscillation to appear and become large towards the root. Such effects show that while high Λ_{LE} has the effect of stabilizing wake oscillations for untapered wings, the combination of wing taper and sweep can promote wake unsteadiness.

For instance, at $\alpha = 18^\circ$ the wake is steady for $\lambda = 0.7$ with long steady streamwise vortices developing from both LE and TE. At $\lambda = 0.5$, unsteadiness appears with vortex rolls at the wing tip, with wake shedding appearing for $\lambda = 0.27$. We quantify the wing taper effect in figure 10(*b*). For instance, for the wings with $\lambda \geq 0.7$ at $\alpha = 18^\circ$, the flow is steady and $\|\boldsymbol{u}'\|_2$ is negligible in the wake. At $\alpha = 22^\circ$, $\|\boldsymbol{u}'\|_2$ is small for untapered wings, increasing considerably in magnitude and spanwise length as the taper ratio decreases. For highly swept tapered wings, the flow fluctuations are exhibited at the tip, further appearing over the midspan for the lower taper ratios.

The unsteady vortices exhibited in the wakes of tapered wings with high LE sweep angles behave as vortex-shedding structures, as shown by the probed u_y in the wake in figure 10(*c*). For $\lambda = 0.7$, the vortices appear as a consistent flow oscillation departing from the wing tip. For $\lambda = 0.27$, the wake is dominated by spanwise-aligned roll structures that occupy a large portion of the wingspan. As these structures develop from the wingspan region near the wing tip, which has a reduced chord length, their frequency $St \approx 0.15$ is slightly higher than the shedding frequency of untapered wings.

The sectional lift distributions around tapered wings with high LE sweep, seen in figure 7(*d*), show how wing taper substantially increases the root contribution to the overall lift. Backward-swept wings have a higher contribution of lift from the root region due to the pair of vortical structures near the midspan that attach closer to the wing surface (Zhang & Taira 2022) similar to the structures shown in figure 8(*a*). For tapered wings, the combined effect of the midspan vortex pair and the development of shedding structures near the wing results in a considerable increase of the overall lift over the entire wingspan for the $\lambda = 0.27$ wing.

4. Conclusions

We have examined the influence of taper and sweep on the dynamics of wake structures for finite NACA 0015 wings with straight-cut tip at a Reynolds number of 600 and a Mach number 0.1. For this study, we performed an extensive campaign of direct numerical simulations of flows over half-span wings with symmetry boundary condition imposed at the wing root. The present numerical study spans over a wide parameter space with angles of attack between $14^\circ \leq \alpha \leq 22^\circ$, aspect ratios $sAR = 1$ and 2, LE sweep angles $0^\circ \leq \Lambda_{LE} \leq 50^\circ$ and taper ratios between $0.27 \leq \lambda \leq 1$. This parameter space was chosen to characterize the effects of wing taper as well as the LE and TE sweep angles on the wake dynamics.

Through direct numerical simulations, we observe that the flow over unswept and untapered wings forms a strong tip vortex, which interacts with the spanwise vortex detaching from the wing surface at the root region. This flow yields a 3-D and unsteady wake for all angles of attack considered herein. Untapered and swept wings are observed to advect the shedding region towards the wing tip for lower angles of sweep. At higher sweep angles, the wake oscillations are attenuated, yielding a steady wake around wings at lower angles of attack.

Wing taper has a strong influence on the wake dynamics. For tapered wings, the LE and TE are not parallel and have a distinct influence on the flow structures within the stalled flow region. For tapered wings with unswept LE and forward-swept TE, taper concentrates shedding structures towards the wing root and yields a broadband spectral content downstream in the wake as a result of increased mixing in that region. Beyond the unsteady wake shedding, the tip vortex is heavily affected by wing taper, reducing its length considerably for tapered wings, as the chord length decreases towards the tip.

For tapered wings with backward-swept LE and unswept TE, the spanwise length where wake unsteadiness is observed increases as shedding is promoted over a larger portion of the wingspan. For this type of tapered wing planform, in contrast to the forward-swept wing effect, the peak of wake unsteadiness moves towards the wing tip region for lower taper ratios. Moreover, for wings with high LE sweep, although the flow is steady for $\lambda = 1$, taper causes wake unsteadiness to appear. The wake oscillations develop near the wing tip for moderate taper ratios. For low λ, wings with high LE sweep angles exhibit strong wake-shedding structures occupying a large portion of the wingspan.

Through the detailed analysis of the wake structures, we also provide a map that classifies the wake behaviour of tapered wings associating the behaviour with the wing planform geometry and the angle of attack. The map provides a unique description of the overall flow physics of the wakes around tapered wings and reveals, for each semi aspect ratio and angle of attack, how the steady–unsteady flow behaviour is related to the wing taper and LE sweep angle. The present study shows the effect of taper, as well as the effects of LE and TE sweep and evaluates its impact on the formation of the wake structures.

Lastly, we show how the wing taper affects the aerodynamic forces over the wing. We show that wings with the same taper ratio may present distinct overall lift and aerodynamic performance, as these characteristics are also influenced by the LE sweep of the wing. Our findings show that the combination of wing taper and high LE sweep can considerably improve lift and the aerodynamic performance of the wing in laminar post-stall flows conditions. The present insights gained into the effect of wing taper in the absence of turbulence serve as a stepping stone for future efforts that aim to study, interpret and control higher-Reynolds-number post-stall flows over tapered wings.

Acknowledgements. The first author thanks T.R. Ricciardi and K. Zhang for enlightening discussions. Computational resources were provided by the High Performance Computing Modernization Program at the US Department of Defense and the Texas Advanced Computing Center.

Funding. We acknowledge the support from the US Air Force Office of Scientific Research (programme manager: Dr G. Abate; grant: FA9550-21-1-0174).

Declaration of interest. The authors report no conflict of interest.

Author ORCIDs.
Jean Hélder Marques Ribeiro https://orcid.org/0000-0002-8613-9593;
Anton Burtsev https://orcid.org/0000-0002-8268-9088;
Michael Amitay https://orcid.org/0000-0003-1366-0406;
Vassilios Theofilis https://orcid.org/0000-0002-7720-3434;
Kunihiko Taira https://orcid.org/0000-0002-3762-8075.

Appendix A. Grid verification

We verify the convergence of grid resolution for the numerical results using a wing with $(sAR, \alpha, \Lambda_{LE}, \lambda) = (2, 22^\circ, 40^\circ, 0.27)$. This planform combines a high LE sweep

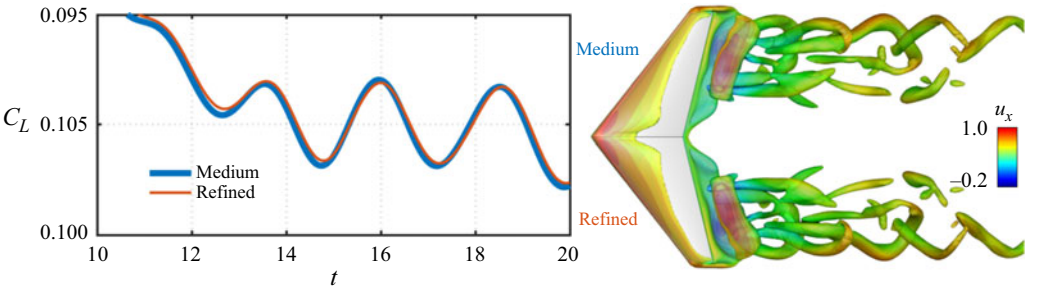

Figure 11. Lift coefficient over time and instantaneous flow-field structures visualized using $Q = 1$ coloured by instantaneous velocity component u_x at the lift peak for the two sets of meshes used for grid verification for the wing with $(sAR, \alpha, \Lambda_{LE}, \lambda) = (2, 22^\circ, 40^\circ, 0.27)$.

angle and the lowest taper ratio considered in the present study. Herein, we report the aerodynamic forces through their lift coefficients C_L. Two meshes are used for verification: a medium and a refined mesh. The medium mesh refinement is the one used throughout the present work. This mesh has 80 grid points on both pressure and suction sides of the wing and 48 grid points along the wingspan, with a total of approximately 3.1×10^6 control volumes. The refined mesh has 120 grid points on pressure and suction sides, with 64 grid points along the wingspan, resulting in approximately 4.3×10^6 control volumes in total. For the refined mesh we have increased the temporal resolution by setting the CFL number to 0.5. The quality of our medium mesh is assessed through the forces exerted over the wing and the instantaneous vortical elements as shown in figure 11.

Appendix B. A portfolio of flow fields around tapered wings

In this appendix, we provide flow-field visualizations of the wake structures around all tapered wings considered in the present study. Flows around $sAR = 1$ wings at $\alpha = 14^\circ$, 18° and 22° are shown in figures 12, 13 and 14, respectively. Similarly, flows around $sAR = 2$ wings at $\alpha = 14^\circ$, 18° and 22° are shown in figures 15, 16 and 17, respectively. All flows are visualized using isosurfaces of $Q = 1$, coloured by the streamwise velocity u_x.

Appendix C. Force element analysis

Force element analysis (Chang 1992) is a method used to identify vortical structures emerging near the wake that play a significant role in exerting aerodynamic loads over the wing. We note that force element theory is similar in spirit to other force element methods derived through a variational approach (Quartapelle & Napolitano 1983), as well as to vortex force maps (Li, Zhao & Graham 2020) and force partition approaches (Menon & Mittal 2021). The present force element analysis was previously employed to analyse incompressible flows over wings in multiple configurations (Lee *et al.* 2012; Zhang *et al.* 2020*b*; Zhang, Shah & Bilgen 2022; Zhang & Taira 2022).

Initially, we define an auxiliary potential with a specific boundary condition of $-\boldsymbol{n} \cdot \nabla\phi_i = \boldsymbol{n} \cdot \boldsymbol{e}_i$ set on the wing surface, where ϕ is the auxiliary potential, $\boldsymbol{n}$ is the unit wall normal vector and $\boldsymbol{e}_i$ is the unit vector in the ith direction. The inner product of the Navier–Stokes equations with $\nabla\phi$ and performing an integral over the fluid domain, the forces exerted in the ith direction may be expressed as

$$F_i = \int_V \boldsymbol{\omega} \times \boldsymbol{u} \cdot \nabla\phi_i \, \mathrm{d}V + \frac{1}{Re} \int_S \boldsymbol{\omega} \times \boldsymbol{n} \cdot (\nabla\phi_i + \boldsymbol{e_i}) \, \mathrm{d}S, \tag{C1}$$

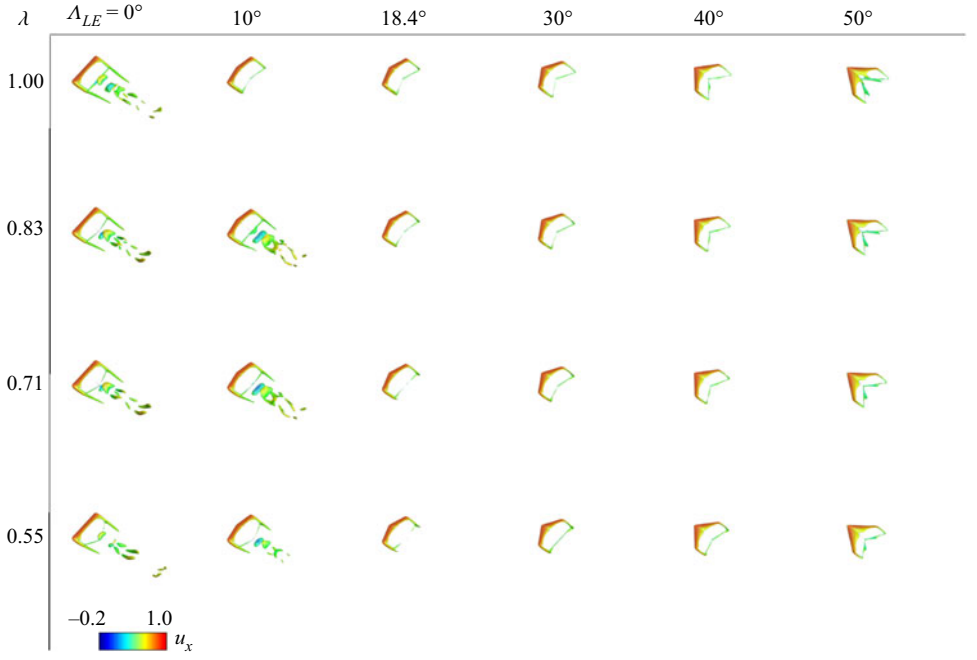

Figure 12. Instantaneous flow fields around wings of $sAR = 1$ at $\alpha = 14°$ visualized using isosurfaces of $Q = 1$ coloured by streamwise velocity u_x.

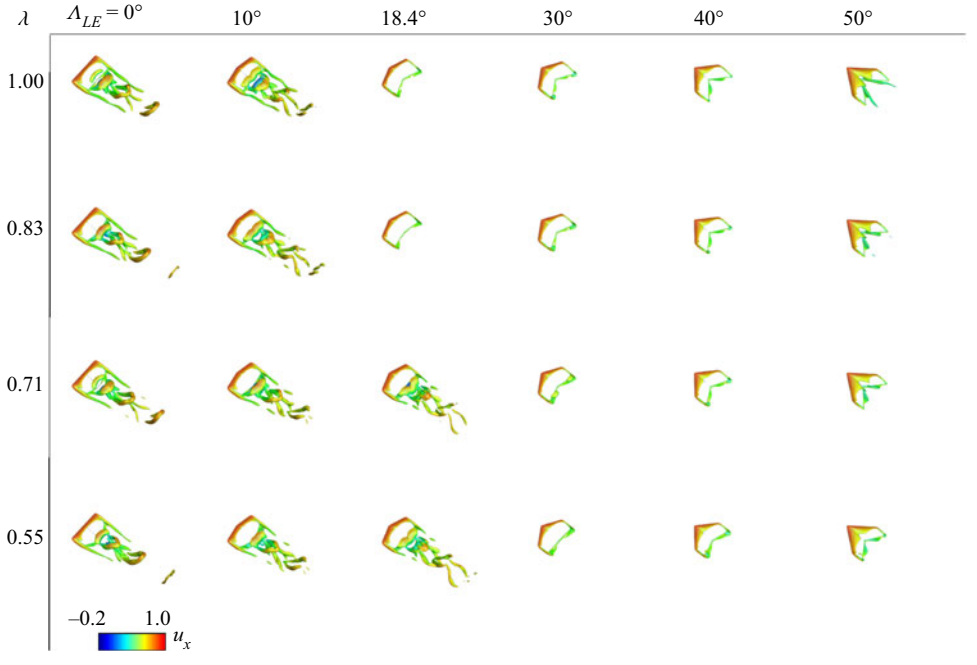

Figure 13. Instantaneous flow fields around wings of $sAR = 1$ at $\alpha = 18°$ visualized using isosurfaces of $Q = 1$ coloured by streamwise velocity u_x.

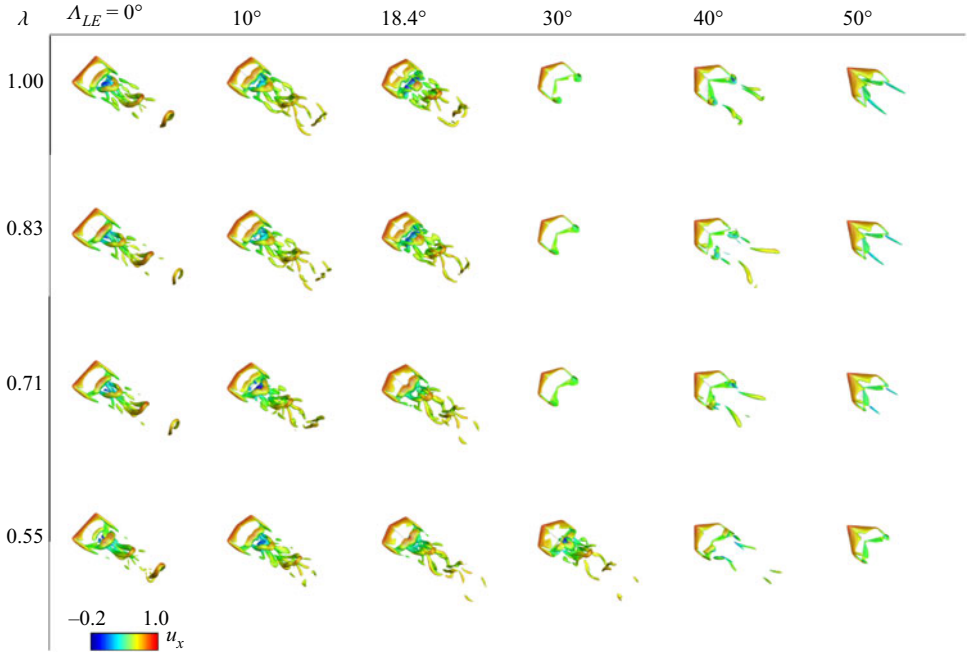

Figure 14. Instantaneous flow fields around wings of $sAR = 1$ at $\alpha = 22°$ visualized using isosurfaces of $Q = 1$ coloured by streamwise velocity u_x.

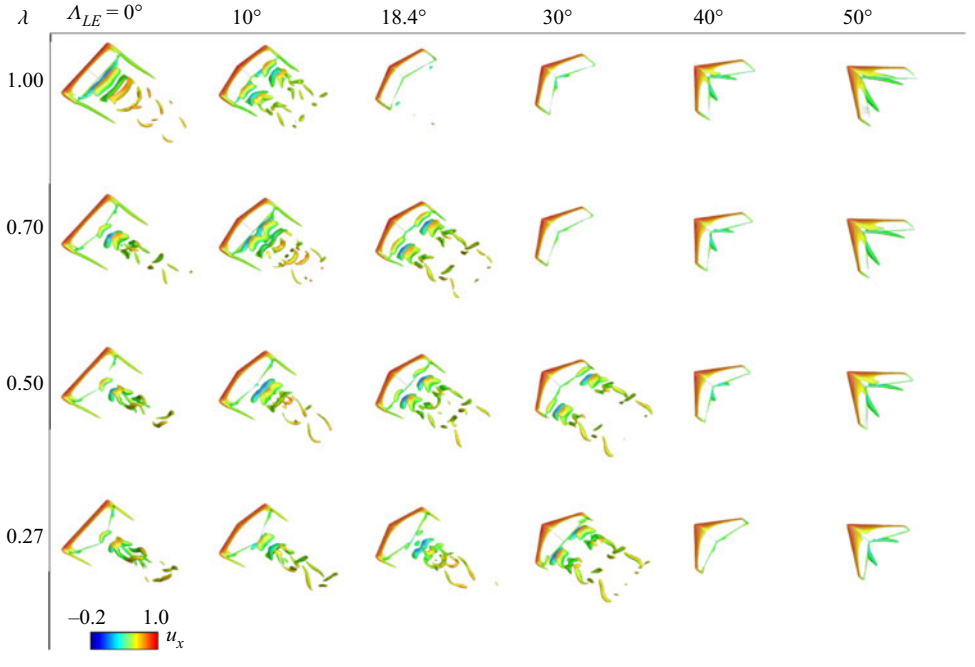

Figure 15. Instantaneous flow fields around wings of $sAR = 2$ at $\alpha = 14°$ visualized using isosurfaces of $Q = 1$ coloured by streamwise velocity u_x.

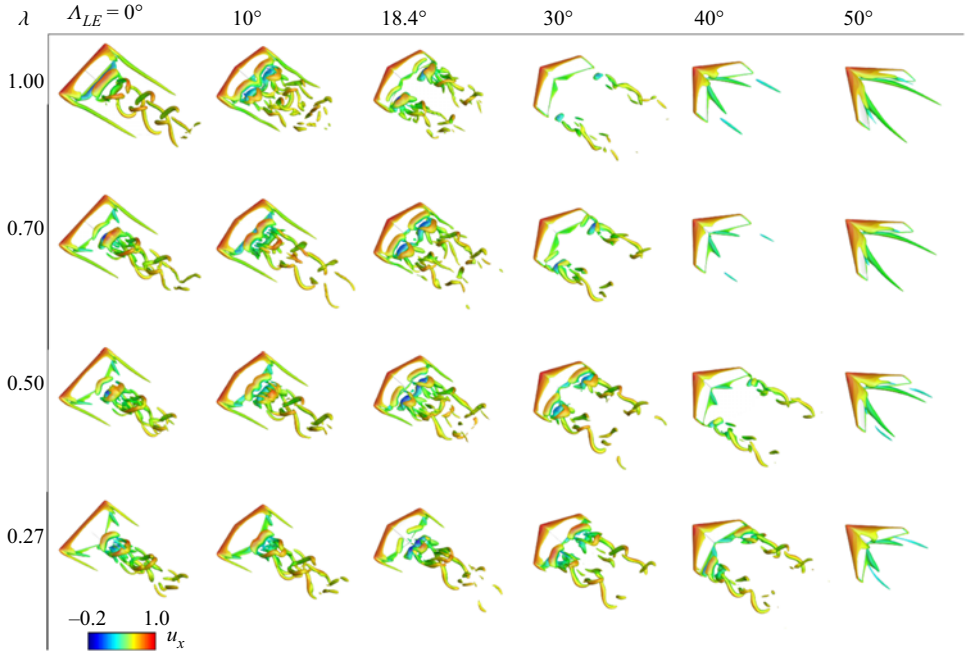

Figure 16. Instantaneous flow fields around wings of $sAR = 2$ at $\alpha = 18°$ visualized using isosurfaces of $Q = 1$ coloured by streamwise velocity u_x.

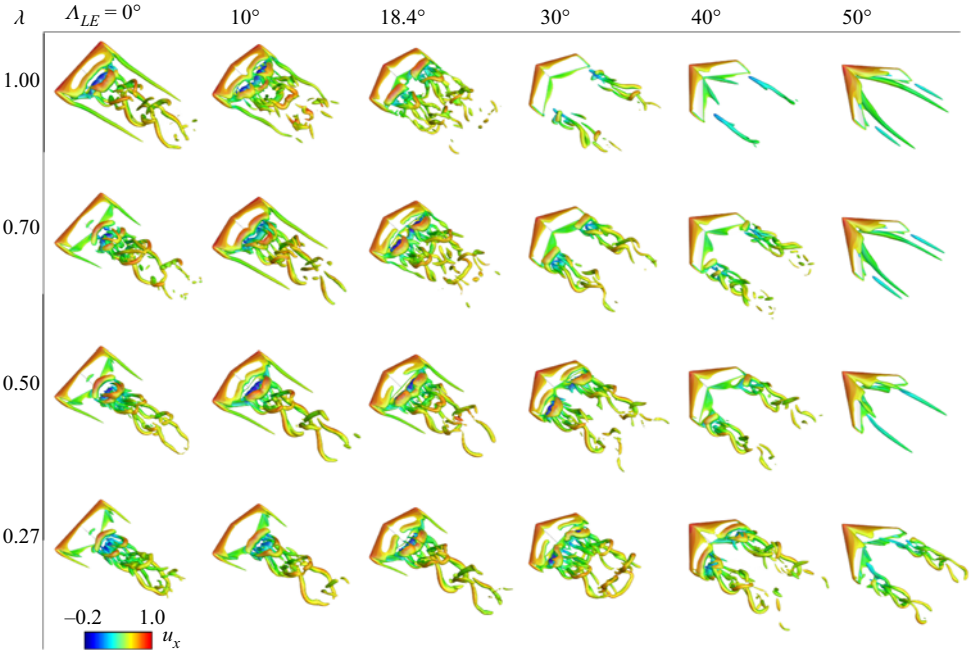

Figure 17. Instantaneous flow fields around wings of $sAR = 2$ at $\alpha = 22°$ visualized using isosurfaces of $Q = 1$ coloured by streamwise velocity u_x.

where the first integral represents the volume force elements and the second integral term is comprised of the surface force elements. For $Re_c = 600$ flows, the volume elements are responsible for the major contribution to the total force over the wing. We note that the auxiliary potential velocity field ϕ_i decays rapidly far from the surface. For this reason, the structures that have a higher contribution to lift are the ones that emerge near the surface.

To visualize the vortical structures associated with lift generation, one can take the Hadamard product of $\nabla\phi_i$ and the Lamb vector $(\boldsymbol{\omega} \times \boldsymbol{u})$, as shown in figure 8. The resulting $(\boldsymbol{u} \times \boldsymbol{\omega}) \cdot \nabla\phi_y$ variable is often called the lift element. Lastly, we recall that the force element theory used herein considers incompressible Navier–Stokes equations. Nevertheless, important insights into the flow structures may still be obtained for weakly compressible flows, such as the ones considered herein and in previous studies as well (Ribeiro *et al.* 2022).

References

Abbott, I.H. & Von Doenhoff, A.E. 1959 *Theory of Wing Sections: Including a Summary of Airfoil Data*. Dover.

Ananda, G.K., Sukumar, P.P. & Selig, M.S. 2015 Measured aerodynamic characteristics of wings at low Reynolds numbers. *Aerosp. Sci. Technol.* **42**, 392–406.

Anderson, R.F. 1936 Determination of the characteristics of tapered wings. *Tech. Rep.* NACA-TR-572. NASA Langley.

Anderson, J.D. 1999 *Aircraft Performance and Design*. WCB/McGraw-Hill.

Anderson, J.D. 2010 *Fundamentals of Aerodynamics*. McGraw-Hill.

Bippes, H. & Turk, M. 1980 Windkanalmessungen in einem Rechteckflügel bei anliegender und abgelöster Strömung. *Tech. Rep.* 251-80 A 18. DFVLR Forschungsbericht IB.

Birch, D., Lee, T., Mokhtarian, F. & Kafyeke, F. 2004 Structure and induced drag of a tip vortex. *J. Aircraft* **41** (5), 1138–1145.

Black, J. 1956 Flow studies of the leading edge stall on a swept-back wing at high incidence. *Aeronaut. J.* **60** (541), 51–60.

Braza, M., Faghani, D. & Persillon, H. 2001 Successive stages and the role of natural vortex dislocations in three-dimensional wake transition. *J. Fluid Mech.* **439**, 1–41.

Breitsamter, C. & Laschka, B. 2001 Vortical flowfield structure at forward swept-wing configurations. *J. Aircraft* **38** (2), 193–207.

Brès, G.A., Ham, F.E., Nichols, J.W. & Lele, S.K. 2017 Unstructured large-eddy simulations of supersonic jets. *AIAA J.* **55** (4), 1164–1184.

Buchholz, J.H.J. & Smits, A.J. 2006 On the evolution of the wake structure produced by a low-aspect-ratio pitching panel. *J. Fluid Mech.* **546**, 433–443.

Burtsev, A., He, W., Hayostek, S., Zhang, K., Theofilis, V., Taira, K. & Amitay, M. 2022 Linear modal instabilities around post-stall swept finite wings at low Reynolds numbers. *J. Fluid Mech.* **944**, A6.

Burtsev, A., Theofilis, V., Ribeiro, J.H.M., Taira, K., Neal, J.M. & Amitay, M. 2023 Wake dynamics of tapered wings. Part III: triglobal linear stability analysis. *AIAA Paper* 2023-2299.

Chang, C.-C. 1992 Potential flow and forces for incompressible viscous flow. *Proc. R. Soc. Lond.* A **437** (1901), 517–525.

Dallmann, U.C. 1988 Three-dimensional vortex structures and vorticity topology. *Fluid Dyn. Res.* **3** (1–4), 183–189.

Délery, J.M. 2001 Robert Legendre and Henri Werlé: toward the elucidation of three-dimensional separation. *Annu. Rev. Fluid Mech.* **33**, 128.

Devenport, W.J., Rife, M.C., Liapis, S.I. & Follin, G.J. 1996 The structure and development of a wing-tip vortex. *J. Fluid Mech.* **312**, 67–106.

DeVoria, A.C. & Mohseni, K. 2017 On the mechanism of high-incidence lift generation for steadily translating low-aspect-ratio wings. *J. Fluid Mech.* **813**, 110–126.

Dong, L., Choi, K.-S. & Mao, X. 2020 Interplay of the leading-edge vortex and the tip vortex of a low-aspect-ratio thin wing. *Exp. Fluids* **61** (9), 1–15.

Durante, D., Rossi, E. & Colagrossi, A. 2020 Bifurcations and chaos transition of the flow over an airfoil at low Reynolds number varying the angle of attack. *Commun. Nonlinear Sci. Numer. Simul.* **89**, 105285.

EDSTRAND, A.M., SUN, Y., SCHMID, P.J., TAIRA, K. & CATTAFESTA, L.N. 2018 Active attenuation of a trailing vortex inspired by a parabolized stability analysis. *J. Fluid Mech.* **855**, R2.

ELDREDGE, J.D. & JONES, A.R. 2019 Leading-edge vortices: mechanics and modeling. *Annu. Rev. Fluid Mech.* **51**, 75–104.

FALKNER, V.M. 1950 Sweepback and wing taper: the effect of sweepback on the lift, drag, and aerodynamic centre of a tapered wing. *Aircraft Engng Aerosp. Technol.* **22** (10), 296–300.

FRANCIS, M.S. & KENNEDY, D.A. 1979 Formation of a trailing vortex. *J. Aircraft* **16** (3), 148–154.

FREUND, J.B. 1997 Proposed inflow/outflow boundary condition for direct computation of aerodynamic sound. *AIAA J.* **35** (4), 740–742.

FREYMUTH, P., FINAISH, F. & BANK, W. 1987 Further visualization of combined wing tip and starting vortex systems. *AIAA J.* **25** (9), 1153–1159.

GASTER, M. 1967 The structure and behaviour of laminar separation bubbles. *AGARD* CP-4.

GREEN, S.I. & ACOSTA, A.J. 1991 Unsteady flow in trailing vortices. *J. Fluid Mech.* **227**, 107–134.

GURSUL, I., GORDNIER, R. & VISBAL, M. 2005 Unsteady aerodynamics of nonslender delta wings. *Prog. Aerosp. Sci.* **41** (7), 515–557.

GURSUL, I. & WANG, Z. 2018 Flow control of tip/edge vortices. *AIAA J.* **56** (5), 1731–1749.

HARPER, C.W. & MAKI, R.L. 1964 A review of the stall characteristics of swept wings. *Tech. Rep.* NASA/TN D-2373. NASA, Washington, DC.

HE, W., GIORIA, R.S., PÉREZ, J.M. & THEOFILIS, V. 2017*a* Linear instability of low Reynolds number massively separated flow around three NACA airfoils. *J. Fluid Mech.* **811**, 701–741.

HE, W., TENDERO, J.A., PAREDES, P. & THEOFILIS, V. 2017*b* Linear instability in the wake of an elliptic wing. *Theor. Comput. Fluid Dyn.* **31**, 483–504.

HOARAU, Y., BRAZA, M., VENTIKOS, Y., FAGHANI, D. & TZABIRAS, G. 2003 Organized modes and the three-dimensional transition to turbulence in the incompressible flow around a NACA 0012 wing. *J. Fluid Mech.* **496**, 63–72.

HORNUNG, H.G. & PERRY, A.E. 1984 Some aspects of three-dimensional separation. Part I. Streamsurface bifurcations. *Z. Flugwiss. Weltraumforsch.* **8**, 77–87.

HORTON, H.P. 1968 Laminar separation bubbles in two and three dimensional incompressible flow. PhD thesis, Queen Mary University of London.

HUANG, Y., VENNING, J., THOMPSON, M.C. & SHERIDAN, J. 2015 Vortex separation and interaction in the wake of inclined trapezoidal plates. *J. Fluid Mech.* **771**, 341–369.

HUANG, R.F., WU, J.Y., JENG, J.H. & CHEN, R.C. 2001 Surface flow and vortex shedding of an impulsively started wing. *J. Fluid Mech.* **441**, 265–292.

HUNT, J.C.R., ABEL, C.J., PETERKA, J.A. & WOO, H. 1978 Kinematic studies of the flows around free or surface-mounted obstacles; applying topology to flow visualization. *J. Fluid Mech.* **86** (1), 179–200.

HUNT, J.C.R., WRAY, A.A. & MOIN, P. 1988 Eddies, streams, and convergence zones in turbulent flows. In *Proceedings of the Summer Program, Center for Turbulence Research*, Stanford, CA, pp. 193–208.

IRVING, H.B. 1937 Some notes on tapered wings: the effects of brake flaps, taper and 'sweep' on stalling. *Aircraft Engng Aerosp. Technol.* **9** (2), 31–36.

JEONG, J. & HUSSAIN, F. 1995 On the identification of a vortex. *J. Fluid Mech.* **285**, 69–94.

KHALIGHI, Y., HAM, F., NICHOLS, J., LELE, S.K. & MOIN, P. 2011 Unstructured large eddy simulation for prediction of noise issued from turbulent jets in various configurations. *AIAA Paper* 2011–2886.

LEE, J.-J., HSIEH, C.-T., CHANG, C.-C. & CHU, C.-C. 2012 Vorticity forces on an impulsively started finite plate. *J. Fluid Mech.* **694**, 464–492.

LI, J., ZHAO, X. & GRAHAM, M. 2020 Vortex force maps for three-dimensional unsteady flows with application to a delta wing. *J. Fluid Mech.* **900**, A36.

LIN, J.C.M. & PAULEY, L.L. 1996 Low-Reynolds-number separation on an airfoil. *AIAA J.* **34** (8), 1570–1577.

MCCORMICK, B.W. 1995 *Aerodynamics, Aeronautics, and Flight Mechanics*. John Wiley & Sons.

MENON, K. & MITTAL, R. 2021 Quantitative analysis of the kinematics and induced aerodynamic loading of individual vortices in vortex-dominated flows: a computation and data-driven approach. *J. Comput. Phys.* **443**, 110515.

MILLIKAN, C.B. 1936 On the stalling of highly tapered wings. *J. Aerosp. Sci.* **3** (5), 145–150.

MUELLER, T.J. 2001 *Fixed and Flapping Wing Aerodynamics for Micro Air Vehicle Applications*. American Institute of Aeronautics and Astronautics, Inc.

NARASIMHAMURTHY, V.D., ANDERSSON, H.I. & PETTERSEN, B. 2008 Cellular vortex shedding in the wake of a tapered plate. *J. Fluid Mech.* **617**, 355–379.

NAVROSE, , BRION, V. & JACQUIN, L. 2019 Transient growth in the near wake region of the flow past a finite span wing. *J. Fluid Mech.* **866**, 399–430.

NEAL, J.M. & AMITAY, M. 2023 Three-dimensional separation over unswept cantilevered wings at a moderate Reynolds number. *Phys. Rev. Fluids* **8**, 014703.

NEAL, J., BURTSEV, A., RIBEIRO, J.H.M., TAIRA, K., THEOFILIS, V. & AMITAY, M. 2023*a* Similarities in massive separation across Reynolds numbers for swept and tapered finite span wings. Preprint, arXiv:2308.12442.

NEAL, J.M., GARES, B., AMITAY, M., BURTSEV, A., THEOFILIS, V., RIBEIRO, J.H.M. & TAIRA, K. 2023*b* Wake dynamics of tapered wings. Part II: an experimental study. *AIAA Paper* 2023-2298.

PANDI, J.S.S. & MITTAL, S. 2019 Wake transitions and laminar separation bubble in the flow past an Eppler 61 airfoil. *Phys. Fluids* **31** (11), 114102.

PANDI, J.S.S. & MITTAL, S. 2023 Streamwise vortices, cellular shedding and force coefficients on finite wing at low Reynolds number. *J. Fluid Mech.* **958**, A10.

PAULEY, L.L., MOIN, P. & REYNOLDS, W.C. 1990 The structure of two-dimensional separation. *J. Fluid Mech.* **220**, 397–411.

PELLETIER, A. & MUELLER, T.J. 2000 Low Reynolds number aerodynamics of low-aspect-ratio, thin/flat/cambered-plate wings. *J. Aircraft* **37** (5), 825–832.

PERRY, A.E. & HORNUNG, H.G. 1984 Some aspects of three-dimensional separation. Part II. Vortex skeletons. *Z. Flugwiss. Weltraumforsch.* **8**, 155–160.

PICCIRILLO, P.S. & VAN ATTA, C.W. 1993 An experimental study of vortex shedding behind linearly tapered cylinders at low Reynolds number. *J. Fluid Mech.* **246**, 163–195.

PRANDTL, L. 1920 Theory of lifting surfaces. *Tech. Rep.* NACA/TN-9. NASA, Washington, DC.

QUARTAPELLE, L. & NAPOLITANO, M. 1983 Force and moment in incompressible flows. *AIAA J.* **21** (6), 911–913.

RIBEIRO, J.H.M., TAIRA, K., NEAL, J.M., AMITAY, M., BURTSEV, A. & THEOFILIS, V. 2023*a* Wake dynamics of tapered wings. Part I: a computational study. *AIAA Paper* 2023-2297.

RIBEIRO, J.H.M., YEH, C.-A. & TAIRA, K. 2023*b* Triglobal resolvent analysis of swept-wing wakes. *J. Fluid Mech.* **954**, A42.

RIBEIRO, J.H.M., YEH, C.-A., ZHANG, K. & TAIRA, K. 2022 Wing sweep effects on laminar separated flows. *J. Fluid Mech.* **950**, A23.

ROCKWELL, D. 1993 Three-dimensional flow structure on delta wings at high angle-of-attack-experimental concepts and issues. *AIAA Paper* 1993-0550.

ROSSI, E., COLAGROSSI, A., OGER, G. & LE TOUZÉ, D. 2018 Multiple bifurcations of the flow over stalled airfoils when changing the Reynolds number. *J. Fluid Mech.* **846**, 356–391.

SCHEWE, G. 2001 Reynolds-number effects in flow around more-or-less bluff bodies. *J. Wind Engng Ind. Aerodyn.* **8**, 1267–1289.

SOULE, H.A. & ANDERSON, R.F. 1940 Design charts relating to the stalling of tapered wings. *Tech. Rep.* NACA-TR-703. NASA.

TAIRA, K. & COLONIUS, T. 2009 Three-dimensional flows around low-aspect-ratio flat-plate wings at low Reynolds numbers. *J. Fluid Mech.* **623**, 187–207.

TECHET, A.H., HOVER, F.S. & TRIANTAFYLLOU, M.S. 1998 Vortical patterns behind a tapered cylinder oscillating transversely to a uniform flow. *J. Fluid Mech.* **363**, 79–96.

THEOFILIS, V., HEIN, S. & DALLMANN, U.C. 2000 On the origins of unsteadiness and three-dimensionality in a laminar separation bubble. *Phil. Trans. R. Soc. Lond.* A **358**, 3229–324.

TOBAK, M. & PEAKE, D.J. 1982 Topology of three-dimensional separated flows. *Annu. Rev. Fluid Mech.* **14** (1), 61–85.

TOPPINGS, C.E. & YARUSEVYCH, S. 2021 Structure and dynamics of a laminar separation bubble near a wingtip. *J. Fluid Mech.* **929**, A39.

TOPPINGS, C.E. & YARUSEVYCH, S. 2022 Structure and dynamics of a laminar separation bubble near a wing root: towards reconstructing the complete lsb topology on a finite wing. *J. Fluid Mech.* **944**, A14.

TORRES, G.E. & MUELLER, T.J. 2004 Low-aspect-ratio aerodynamics at low Reynolds numbers. *AIAA J.* **42** (5), 865–873.

TRAUB, L.W. 2013 Aerodynamic impact of aspect ratio at low Reynolds number. *J. Aircraft* **50** (2), 626–634.

TRAUB, L.W., BOTERO, E., WAGHELA, R., CALLAHAN, R. & WATSON, A. 2015 Effect of taper ratio at low Reynolds number. *J. Aircraft* **52** (3), 734–747.

VALLES, B., ANDERSSON, H.I. & JENSSEN, C.B. 2002 Oblique vortex shedding behind tapered cylinders. *J. Fluids Struct.* **16** (4), 453–463.

VIDELER, J.J., STAMHUIS, E.J. & POVEL, G.D.E. 2004 Leading-edge vortex lifts swifts. *Science* **306** (5703), 1960–1962.

VISBAL, M.R. & GARMANN, D.J. 2019 Effect of sweep on dynamic stall of a pitching finite-aspect-ratio wing. *AIAA J.* **57** (8), 3274–3289.

WEI, Z., NEW, T.H. & CUI, Y.D. 2018 Aerodynamic performance and surface flow structures of leading-edge tubercled tapered swept-back wings. *AIAA J.* **56** (1), 423–431.

WINKELMAN, A.E. & BARLOW, J.B. 1980 Flowfield model for a rectangular planform wing beyond stall. *AIAA J.* **18** (8), 1006–1008.

YARUSEVYCH, S., SULLIVAN, P.E. & KAWALL, J.G. 2009 On vortex shedding from an airfoil in low-Reynolds-number flows. *J. Fluid Mech.* **632**, 245–271.

YEN, S.-C. & HSU, C.M. 2007 Flow patterns and wake structure of a swept-back wing. *AIAA J.* **45** (1), 228–236.

YEN, S.-C. & HUANG, L.-C. 2009 Flow patterns and aerodynamic performance of unswept and swept-back wings. *J. Fluids Engng* **131** (11), 111101.

YILMAZ, T.O. & ROCKWELL, D. 2012 Flow structure on finite-span wings due to pitch-up motion. *J. Fluid Mech.* **691**, 518–545.

ZHANG, K., HAYOSTEK, S., AMITAY, M., BURSTEV, A., THEOFILIS, V. & TAIRA, K. 2020*a* Laminar separated flows over finite-aspect-ratio swept wings. *J. Fluid Mech.* **905**, R1.

ZHANG, K., HAYOSTEK, S., AMITAY, M., HE, W., THEOFILIS, V. & TAIRA, K. 2020*b* On the formation of three-dimensional separated flows over wings under tip effects. *J. Fluid Mech.* **895**, A9.

ZHANG, K., SHAH, B. & BILGEN, O. 2022 Low-Reynolds-number aerodynamic characteristics of airfoils with piezocomposite trailing surfaces. *AIAA J.* **60** (4), 2701–2706.

ZHANG, K. & TAIRA, K. 2022 Laminar vortex dynamics around forward-swept wings. *Phys. Rev. Fluids* **7** (2), 024704.